The Astronomical Journal, 156:29 (24pp), 2018 July https://doi.org/10.3847/1538-3881/aac822

The Grism Lens-amplified Survey from Space (GLASS). XII. Spatially Resolved Galaxy Star Formation Histories and True Evolutionary Paths at $z > 1$*

L. E. Abramson[1], A. B. Newman[2], T. Treu[1], K. H. Huang[3,4], T. Morishita[5], X. Wang[1], A. Hoag[3], K. B. Schmidt[6], C. A. Mason[1], M. Bradač[3], G. B. Brammer[5], A. Dressler[2], B. M. Poggianti[7], M. Trenti[8], and B. Vulcani[7,8]
[1] UCLA, 430 Portola Plaza, Los Angeles, CA 90095, USA; labramson@astro.ucla.edu
[2] The Carnegie Observatories, 813 Santa Barbara Street, Pasadena, CA 91101, USA
[3] UC Davis, 1 Shields Avenue, Davis, CA 95616, USA
[4] Translational and Molecular Imaging Institute, Icahn School of Medicine at Mt. Sinai, 1470 Madison Avenue, New York, NY 10029, USA
[5] Space Telescope Science Institute, 3700 San Martin Drive, Baltimore, MD 21218, USA
[6] Leibniz-Institut für Astrophysik Potsdam, An der Sternwarte 16, D-14482 Potsdam, Germany
[7] INAF–Osservatorio Astronomico di Padova, Vicolo Osservatorio 5, I-35122 Padova, Italy
[8] School of Physics, University of Melbourne, VIC 3010, Australia
Received 2017 October 1; revised 2018 May 21; accepted 2018 May 23; published 2018 June 29

Abstract

Modern data empower observers to describe galaxies as the spatially and biographically complex objects they are. We illustrate this through case studies of four $z \sim 1.3$ systems based on deep, spatially resolved, 17-band + G102 + G141 *Hubble Space Telescope* grism spectrophotometry. Using full-spectrum rest-UV/-optical continuum fitting, we characterize these galaxies' observed ∼kpc-scale structures and star formation rates (SFRs) and reconstruct their history over the age of the universe. The sample's diversity—passive to vigorously star-forming; stellar masses log $M_*/M_\odot = 10.5$ to 11.2—enables us to draw spatiotemporal inferences relevant to key areas of parameter space (Milky Way– to super-M31–mass progenitors). Specifically, we find signs that bulge mass fractions (B/T) and SF history shapes/spatial uniformity are linked, such that higher B/Ts correlate with "inside-out growth" and central specific SFRs that peaked above the global average for all star-forming galaxies at that epoch. Conversely, the system with the lowest B/T had a flat, spatially uniform SFH with normal peak activity. Both findings are consistent with models positing a feedback-driven connection between bulge formation and the switch from rising to falling SFRs ("quenching"). While sample size forces this conclusion to remain tentative, this work provides a proof-of-concept for future efforts to refine or refute it: *JWST*, *WFIRST*, and the 30 m class telescopes will routinely produce data amenable to this and more sophisticated analyses. Such samples spanning representative mass, redshift, SFR, and environmental regimes will be ripe for converting into thousands of subgalactic-scale empirical windows on what individual systems actually looked like in the past, ushering in a new dialogue between observation and theory.

Key words: galaxies: evolution – galaxies: stellar content – galaxies: structure – methods: data analysis

1. Introduction

A core goal of studying galaxy evolution is understanding why a galaxy has a given stellar mass (M_*), star formation rate (SFR), size (r_e), color, structure, and chemical composition at a given time. Large amounts of data describing those properties in different galaxies at different times circumscribe this endeavor: deep and wide ground- and space-based imaging yields censuses to $z \gtrsim 2$—over 75% of cosmic history—complete to below the mass of the modern Milky Way (MW; Grogin et al. 2011; Spitler et al. 2012; Illingworth et al. 2016). Ground- and space-based spectroscopy adds details on stellar populations, (gaseous) metallicities, kinematics, and hydrodynamics to those images (York et al. 2000; Calvi et al. 2011; Brammer et al. 2012; Oemler et al. 2013b; Kelson et al. 2014; Steidel et al. 2014; Kriek et al. 2015; Shapley et al. 2015; Momcheva et al. 2016). Combined, the above form a rich database describing many aspects of the cosmic galaxy ensemble at different snapshots of its existence ready to be compared to the ever-advancing numerical and semi-analytic models that seek to explain them (e.g., Benson 2012; Hopkins et al. 2014; Vogelsberger et al. 2014; McAlpine et al. 2016).

Indeed, at the population level, the mean and dispersion of many of the above spatially unresolved properties are probably well enough known to require little further empirical investigation. With samples of thousands of log $M_* \gtrsim 10$, $z \lesssim 2$ systems, statistical uncertainties may no longer impede our understanding as much as systematic interpretive issues regarding how/whether population constraints bear on the physics that shapes the development of a galaxy—the objective stated above.[9]

This problem arises from the inescapable fact that the data are cross-sectional, capturing different systems at different times, while the physics is longitudinal, affecting the same systems at different times. This disconnect allows different models to describe the same (uncontested) observations. Projections of the size–SFR–mass plane provide rich grounds for such debate (Peng et al. 2010; Gladders et al. 2013; Pacifici et al. 2013, 2016; Kelson 2014; Zolotov et al. 2015; Abramson et al. 2016; Abramson & Morishita 2018; Barro et al. 2017b; Fagioli et al. 2016; Lilly & Carollo 2016; Morishita et al. 2017; Oemler et al. 2017): Whether, for example, red galaxies' small

* Uses data from the Keck I 10 m telescope at Maunakea, Hawai'i.

[9] These statements do not hold for phenomena related to galaxies' environments, circumgalactic media, neutral gas, or stellar chemical abundances (Z). Comparable constraints in those domains await future surveys by, e.g., the *Square Kilometre Array*, *Prime Focus Spectrograph*, or *WFIRST*.

size compared to blue ones reflects a rapid quenching transformation or merely the universe's density evolution has strong implications for the interplay between galactic structure and star formation.

Progress requires lifting these descriptive degeneracies using different kinds of information, not just more of it (Abramson et al. 2016; Kelson et al. 2016). Principally, higher-resolution observations and inferences may be key.

Observationally, despite the breadth and depth of current surveys, galaxies are still typically analyzed as monolithic entities with a single stellar mass, SFR, or metallicity. As such, they are condensed to points in parameter space through or near which more than one physical model can pass.

The advent of large samples of spatially resolved integral field unit (IFU) spectroscopy is changing this norm. These data transform galaxies into many stellar populations corresponding to many mass surface densities/metallicities, challenging models to reproduce distributions for individual objects, not just integrated quantities (Blanc et al. 2009; Förster Schreiber et al. 2009; Cappellari et al. 2011; Sánchez et al. 2012; Allen et al. 2015; Bundy et al. 2015; Magdis et al. 2016; Goddard et al. 2017; Mason et al. 2017; Poggianti et al. 2017).

Inferentially, empirical reconstructions of galaxy star formation histories (SFHs) are adding new temporal resolution to shed light on a system's full growth curve, not just its integral (M_*) or current derivative (SFR($t_{\rm obs}$)). Such techniques have been used to estimate galaxies' light-/mass-weighted ages (constraining quenching timescales and late-time star formation; Tinsley 1968; Dressler & Gunn 1983; Couch & Sharples 1987; Poggianti et al. 1999, 2013; Kelson et al. 2001; Kauffmann et al. 2003; Dressler et al. 2004; Treu et al. 2005; Fritz et al. 2007, 2014; Kriek et al. 2008; Domínguez Sánchez et al. 2016), but they also provide insight into more abstract questions, such as the extended role of environment (Trager et al. 2000; Thomas et al. 2005; Kelson et al. 2006; Guglielmo et al. 2015; McDermid et al. 2015), whether galaxy histories are self-similar (Pacifici et al. 2016), how their parameterization affects population-level inferences (Tinsley 1968; Gallagher et al. 1984; Oemler et al. 2013a; Ciesla et al. 2017; Iyer & Gawiser 2017), and whether established ways of classifying galaxies or placing them in dark matter halos need rethinking (Weisz et al. 2014; Dressler et al. 2016; Dressler et al. 2018).

Expanding the space in which we think about galaxies and "longitudinalizing" their cross-sectional snapshots have great promise individually, but combining them is optimal. While higher spatial resolution data allow for more realistic descriptions, reconstructing SFHs for parts of galaxies would enable full spatiospectral projections of what individual systems actually looked like in the past (as opposed to, e.g., abundance matching–based inferences; van Dokkum et al. 2013; Morishita et al. 2015).[10] Unfortunately, due to resolution and signal-to-noise ratio (S/N) requirements, suitable IFU surveys reaching stellar continua are limited to the local universe (Ma et al. 2014; McDermid et al. 2015; Goddard et al. 2017), far from the peak of stellar mass production/galaxy growth ($0.7 \lesssim z \lesssim 2$; Madau & Dickinson 2014). Yet by brightening and extending sources by ∼2–10×, gravitational lensing can help bypass this constraint.

Combined with the native sensitivity and spatial resolution of the *Hubble Space Telescope* (*HST*), lensing—especially by foreground galaxy clusters—yields unprecedented views into galaxies at the peak of cosmic activity (e.g., Wuyts et al. 2012a, 2012b), resolving their star formation and gas/stellar properties in such detail as to meaningfully challenge theory (Wuyts et al. 2014; Jones et al. 2015; Newman et al. 2015; Johnson et al. 2017a, 2017b; Mason et al. 2017; Rigby et al. 2017; Toft et al. 2017; Wang et al. 2017). The Grism Lens-Amplified Survey from Space (GLASS; Schmidt et al. 2014; Treu et al. 2015) builds on this foundation, turning *HST*'s slitless Wide Field Camera 3 (WFC3) IR grism on the powerful lenses from the Cluster Lensing And Supernova survey with Hubble (CLASH; Postman et al. 2012) and Hubble Frontier Field (HFF; Lotz et al. 2017) campaigns.

Exploiting space's low-IR backgrounds and lack of seeing limitations and lensing's additional resolution and S/N boosts, GLASS provides rest-optical continuum spectra for SFR-unbiased, $z \gtrsim 1$ galaxy samples resolved out to ∼2 half-light radii. These IFU-like data (Vulcani et al. 2015b, 2016, 2017; Wang et al. 2017) enable individual systems' size, mass, and SFR evolution to be inferred over Gyr timescales, providing new spatiotemporal empirical windows on how galaxies wove their way through the cosmic narrative.

Here we use these data to reconstruct the spatially resolved histories of four $z > 1$, log $M_* \gtrsim 10.5$ galaxies spanning a diversity of star formation states from fully passive to strongly star-forming. We then use these inferences to draw links between the systems' observed stellar structures and the shapes of their SFHs. While sample size limits the generality of our conclusions, our analysis represents a first step toward building a new common ground for observational and theoretical studies, providing a proof-of-concept for methods that could be readily applied to representative *JWST*, *WFIRST*, or 30 m class data sets.

We proceed as follows. Section 2 describes the *HST* spectrophotometry and lensing magnification estimates (2.5); Section 3 describes the SFH fitting process; Section 4 describes the integrated (4.1), spatially resolved (4.2), and spatiotemporally resolved (4.3) inferences derived therefrom; and Section 5 describes their astrophysical (5.1) and methodological/theoretical (5.2) implications. Appendices A–E provide further details. Readers comfortable with modern spectral energy distribution (SED) fitting techniques can skip to Section 4.

We take (H_0, Ω_m, Ω_Λ) = (73 km s^{-1} Mpc^{-1}, 0.27, 0.73) and quote AB magnitudes.

2. Data

We combine public GLASS spectroscopy[11] with CLASH and HFF imaging[12,13] to create integrated and spatially resolved SEDs in three radial bins at $|r| \lesssim 2\ r_e$ for four diverse $z \sim 1.3$ galaxies selected for their brightness and spectral quality. Fitting these SEDs provides our SFHs (Section 3). We defer to Schmidt et al. (2014) and Treu et al. (2015) for GLASS's details but review some relevant aspects here.

[10] Of course, any inference can only reflect the contents of an aperture at $t_{\rm obs}$. Since a galaxy's stars and gas may never occupy a given subgalactic-scale aperture at other t, such temporal extrapolations are inescapably complicated. Section 5.2.2 touches on this "noise floor."

[11] https://archive.stsci.edu/prepds/glass/
[12] https://archive.stsci.edu/prepds/clash/
[13] https://archive.stsci.edu/prepds/hff/

Table 1
Basic Source Information

Sight Line	GLASS ID_PA[a]	Tag	R.A. [deg] (J2000)	Decl. [deg] (J2000)	z[b]	$z_{\rm GLASS}$[c]	Magnification (μ)[d]	Pre-survey	F140W$_{\rm GLASS}$[e] (AB)
MACS0744	00660_2	PAS	116.2281	39.46423	1.257 ± 0.005	1.260 ± 0.006	1.87 ± 0.24	CLASH	21.42
MACS1149	00900_1	SSF	177.4089	22.40319	1.021 ± 0.001	1.033 ± 0.007	1.67 ± 0.23	CLASH, HFF	21.22
MACS1423	01916_2	PSB	215.9373	24.06136	1.423 ± 0.002	1.435 ± 0.006	1.52 ± 0.24	CLASH	21.34
MACS2129	00451_2	CSF	322.3719	−7.68199	1.367 ± 0.001	1.368 ± 0.006	1.66 ± 0.24	CLASH	21.72

Notes.
[a] GLASS source number and orientation of the analyzed spectra; "_1" corresponds to the GLASS position angle closest to zero.
[b] Basis of this analysis; from full spectrophotometric fitting (Section 3).
[c] GLASS catalog redshift; error corresponds to a ∼10 pixel LSF FWHM at observed Hα; roughly $\sigma_v = 2000$ km s^{-1}.
[d] From the online calculator (HFF) or the maps of Zitrin et al. (CLASH; Section 2.5).
[e] GLASS catalog SExtractor `MAG_AUTO` estimate.

2.1. GLASS Spectroscopy

GLASS obtained slitless WFC3IR G102 and G141 grism spectra ($\lambda \sim 8800$–16700 Å) covering 10 HFF/CLASH cluster sight lines. To mitigate against nearby object contamination, two spectra were taken per sight line at roughly orthogonal roll angles over 5(G102)+ 2(G141) orbits per orient, reaching similar depths in each grism. The objects studied here have usable data from only one orient (Section 2.2).

A modified 3D *HST* pipeline (Brammer et al. 2012; Momcheva et al. 2016) associates these spectra with objects identified in deeper CLASH/HFF preimaging, subtracts contaminating light from nearby traces, and produces FITS cubes for each source in each grism at each orient. `Type-written text` denotes layers of these files (Appendix A provides a thorough description), but at root, we rely on each source's postage stamps, 2D spectra, and rms and contamination maps. Section 2.3 details how these objects guide 1D spectral extraction.

The GLASS database contains 23,265 objects, 3022 of which have F140W$_{\rm GLASS} \leqslant 24$ and so were inspected and assigned a fiducial spectroscopic redshift ($z_{\rm GLASS}$). All redshifts quoted here are rederived in the analysis (Section 3) but agree with $z_{\rm GLASS}$ within the uncertainties (Table 1).

2.2. Sample Selection

We aim to spectrophotometrically reconstruct spatially resolved SFHs to draw more meaningful longitudinal inferences from cross-sectional data. In scheme, we follow Kelson et al. (2014) and Dressler et al. (2016), Newman et al. (2014), and Domínguez Sánchez et al. (2016), who demonstrated the potential of this approach using similar but spatially integrated data at $z \sim 0.7$, $z \sim 1.8$, and our $z = 1$–1.5 range, respectively.

The critical aspect of these data is that photometry samples the rest-UV/-IR where SFH information is low (current SFR and total M_*, respectively). Meanwhile, spectroscopy covers the high information density rest-optical, containing details on the intermediate-age stellar populations that provide leverage on the path a galaxy took to reach those end points. The highest available spectral resolution ($R_{\rm eff} \gtrsim 70$) is thus present where needed. This said, we diverge from the above studies in that *Spitzer* IRAC's larger point spread function (PSF) precludes us from using those data for spatially resolved photometry.

We stress that, for the case studies possible at this stage, data quality, not quantity, is key. While we will speculate on their broader implications (Sections 4.3 and 5.1), we are not yet so interested in the representativeness of any one finding but rather the potential of what can be learned from these data/methods. Given the critical role of spectroscopy in this exercise, the GLASS database determines sample selection.

From the 2176 sources at $1.0 \leqslant z \leqslant 1.8$, where z is $z_{\rm GLASS}$ or a photometric redshift (Brammer et al. 2008; Castellano et al. 2016; Morishita et al. 2017), we draw 76 sources with F140W$_{\rm GLASS} \leqslant 21.8$. This ensures that important age-sensitive features lie in the grism bandpasses (the 4000 Å break, *G*-band to Mg*b* continuum, and as many Balmer lines as possible), avoids selecting against passive systems lacking a secure (emission line–based) $z_{\rm GLASS}$, and ensures $\langle {\rm S/N} \rangle \approx 10$ per ∼10 pixel resolution element in the (folded) OUTER extractions (see Figure 15 in Appendix A, and Section 2.3). We then select 29 objects with at least one pair of grism spectra with ⩽30% of OUTER pixels contaminated at ⩽30%, where "contaminated" is the ratio of the `CONTAM` to `MODEL` FITS layers (Appendix A). This quality-control cut is arbitrary but balances sample size with avoiding continuum biases from contamination subtraction residuals. (No source has ⩽10% of pixels at ⩽10% contamination.)

Finally, we discard three obvious mergers, 18 poorly sampled sources (1 pixel wide extraction boxes, some of which are stars), one case of bad sky subtraction, two ex post facto–identified low-z interlopers, and one source for which the lognormal SFH failed to converge (Section 3).

This leaves a final sample of four sources. Fortuitously, they constitute a meaningfully diverse cohort of a continuously star-forming (CSF), strongly star-forming (SSF), recently quenched/post-starburst (PSB), and anciently passive (PAS) galaxy. Figure 1 shows these sources and their integrated spectrophotometry. Section 4.1 and Tables 1 and 2 describe them in detail. Though modest ($\langle \mu \rangle \simeq 1.7$), no source would meet the S/N requirements without lensing magnification.

2.3. 1D Spectra

We extract an optimal integrated spectrum and three folded radial spectra from each source. To mimic typical analyses, the former is used to derive total galaxy properties, the latter resolved ones. Summing the spatial extractions produces self-consistent results (Appendix C). Obtaining and analyzing these spectra requires estimating 1D half-light radii, r_e, optimal extraction spatial weights, and line-spread functions (LSFs)

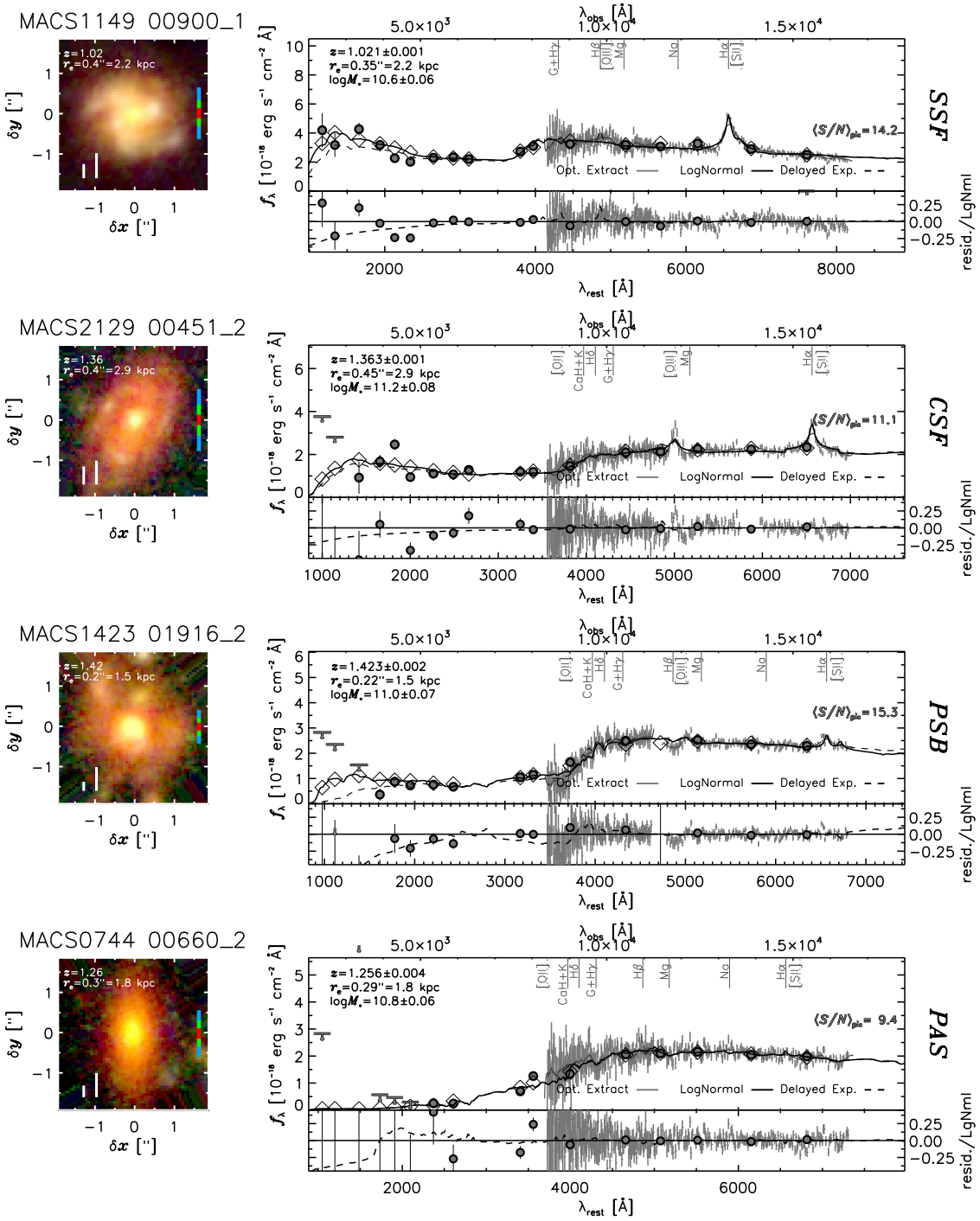

Figure 1. Color CLASH/HFF stamps and optimal GLASS spectra of the four sample objects (Table 1), ordered by decreasing sSFR from top to bottom. The smaller white scale bar on each $\sim 4'' \times 4''$ image shows r_e; the larger shows 5 kpc at the source redshift. Multicolored scale bars at right show the location/width of the radial spectral zones (Section 2.3) color-coded as in Figure 2 and all further plots. CLASH/HFF photometry/2σ limits are denoted by circles and arrows, respectively, with open diamonds showing the *pyspecfit* model values assuming lognormal (solid) or delayed exponential (dashed lines) SFHs. Spectra are plotted as their 1σ uncertainty interval at each λ. Numbers at the red ends of the spectra give mean per-pixel S/N. Other integrated physical parameters are listed at the top left.

using the GLASS postage stamps (DIRECT_IMAGE; stacks of all WFC3IR preimaging).

To avoid including near neighbors whose spectra are removed by the pipeline, this process entails some modeling. We collapse the central 20×20 pixels ($\sim 10 \times 10$ kpc) of each image along the spectral axis (to obtain the target's spatial profile) or spatial axis (to obtain the LSF from its morphology). We then fit Moffat functions to these profiles—which reach beyond bulges but not to outer disks (Figure 1)—and extrapolate to extend them to the full 60 pixel stamp size. The LSF is used in SED fitting (Section 3); the spatial profile defines the optimal extraction weights (Horne 1986) and r_e, on which the radial extractions are based.

Figure 2 shows each source's CLASH/HFF stamps, 1D r_e and 2D half-light radii, 2D spectra, radial extraction zones, and corresponding 1D spectra. The radial bins are

Table 2
Derived Integrated Properties from Optimal Extractions

Tag	$\log M_*/M_\odot$[a,b]	$\log \mathrm{SFR}/M_\odot\ \mathrm{yr}^{-1}$[a,b]	r_e (kpc)[b]	$r_{e,2D}$ (kpc)[b,c]	A_V (mag)[a]	(T_0, τ) (ln Gyr)[a]	(age, τ_{exp}) (Gyr)
PAS	10.83 ± 0.06 (0.17)	<-1.18[d]	1.76 ± 0.11	2.15 ± 0.13	0.09 ± 0.09	$(1.03 \pm 0.08, 0.13 \pm 0.03)$	$(1.48 \pm 0.25, 0.04 \pm 0.05)$
SSF	10.57 ± 0.06 (0.06)	1.40 ± 0.06 (0.12)	2.20 ± 0.14	2.86 ± 0.19	1.06 ± 0.02	$(1.64 \pm 0.00, 0.10 \pm 0.00)$	$(0.70 \pm 0.09, 0.24 \pm 0.04)$
PSB	10.95 ± 0.07 (0.12)	0.54 ± 0.10 (0.93)	1.54 ± 0.11	2.88 ± 0.21	0.41 ± 0.05	$(1.21 \pm 0.01, 0.10 \pm 0.00)$	$(0.42 \pm 0.09, 0.06 \pm 0.02)$
CSF	11.15 ± 0.07 (0.10)	1.59 ± 0.11 (0.39)	2.94 ± 0.20	3.61 ± 0.24	1.19 ± 0.12	$(1.32 \pm 0.35, 0.68 \pm 0.31)$	$(3.51 \pm 0.66, 1.42 \pm 0.60)$

Notes.
[a] Lognormal SFHs. Parentheses show summed INNER + 2 MIDDLE + 2 OUTER M_* or SFR errors; delayed exponential M_* but not necessarily SFR are consistent (Figure 4, Table 4).
[b] Magnification-corrected (Table 1); uncertainties incorporate μ errors.
[c] SExtractor half-light radius.
[d] 2σ limit.

1. *INNER:* $|r/r_e| \leqslant 0.4$;
2. *MIDDLE:* $0.4 < |r/r_e| \leqslant 1.0$;
3. *OUTER:* $1.0 < |r/r_e| \leqslant 2.0$;

where the MIDDLE and OUTER bins are reflected over the GLASS pipeline-output spectral centerline (YTRACE; galactocentric radius $r \equiv y - \mathrm{YTRACE} = 0$) and averaged before fitting. Bin widths are thus 0.8, 2×0.6, and $2 \times 1.0\, r_e$, respectively. While somewhat arbitrary and subject to pixelation, these zones were chosen to counter decreasing S/N(r) while preserving spectral line shapes. Each zone's 1D spectrum is the mean of all unmasked pixels (SCI > 0, CONTAM/SCI < 0.01; Appendix A) in the CONTAM-subtracted 2D SCI spectrum at each λ. Uncertainties are the identical (quadrature) sums from the WHT rms map. GLASS 2D spectra are cut from interlaced—not drizzled—mosaics, so all pixels are independent. We find no significant backgrounds.

Note that, as defined, "r_e" is not the half-light radius returned by, e.g., SExtractor or GALFIT (Bertin & Arnouts 1996; Peng et al. 2002) but rather the y extent containing half the light collapsed across x. This is appropriate for defining spectral bins by spatial S/N but underestimates 2D half-light radii. This effect is small except in ID 01916_2 ("PSB"; Figure 2). For consistency, we do not alter this object's extraction windows, which nevertheless reach the 2D half-light radius, but note when the reduced coverage qualitatively affects our conclusions.

Finally, we estimate each zone's LSFs independently to account for galaxy chord profile variations and position angle effects. At G102/141 resolution, PAs near 45° impose a geometric r–λ covariance. This is not a Doppler shift but is instead due to the slitless grisms reproducing an image of the entire source at every wavelength. Such offsets can reach $\sim$3 pixels or 30% LSF FWHM ($\sim$60 Å; $\Delta z \sim 0.005$; Figures 2 and 16).

2.4. Photometry

Each source is covered by 17-band CLASH imaging, with one having supplementary HFF data in seven bands (Table 1). These data reach into the rest UV ($\sim$1500 Å), providing critical leverage on dust and recent star formation.

We incorporate these data by cutting stamps/rms maps for each source from its full, PSF-matched CLASH/HFF mosaic (Morishita et al. 2017), resampled and rotated to the GLASS plate scale/orientation (Appendix A). Resolved photometry is the sum of the cutouts in each radial zone. To match the spectra, INNER data are left as-is, while the upper and lower MIDDLE and OUTER counts are averaged, respectively. For optimal extraction, the zones are summed, weighted by the spatial profile. Since all images are convolved a priori to F160W resolution, the resultant spectrophotometry is effectively aperture-matched. Comparing synthetic F140W magnitudes from the GLASS spectra to broadband fluxes suggests an absolute accuracy of $\pm\sim$30% (1.5σ). Yet relative spectrophotometric agreement is more important in SED fitting. As we correct the photometry for galactic extinction (Schlafly & Finkbeiner 2011),[14] we ultimately normalize the spectra to those data using a single multiplicative constant. (Otherwise, the two data sets are independent; see Section 3 and Appendix B.) Figures 1 and 2 show that subsequent agreement is excellent.

This process yields four "radially resolved" 17-band + G102/141 spectrophotometric data sets per galaxy ready for SPS modeling. Section 4.3.3 and Appendix C discuss how the spatial extractions studied here differ from truly radially representative SEDs. Extant spatially integrated data not used in the modeling serve as cross-checks (Section 4.2).

2.5. Lensing Magnification

Lensing boosts apparent fluxes and sizes. Hence, estimating absolute quantities using those data (M_*, SFR, intrinsic size) requires knowledge of a source's magnification, μ. This is provided by multiple models built for the GLASS cluster sight lines (Zitrin et al. 2009, 2013; Oguri et al. 2010; Jauzac et al. 2014; Johnson et al. 2014; Richard et al. 2014; Grillo et al. 2015; Wang et al. 2015; Hoag et al. 2016; Kawamata et al. 2016; Caminha et al. 2017). Since μ is applied to derived quantities, this step is independent of the preceding.

ID 00900_1 ("SSF") lies in the HFF footprint, so we download its default set public lens model values,[15] discard the extremes, and adopt the mean (1.67) and scatter (0.23; 14%) of the other inferences as μ and its error. The other sources lack HFF coverage, so we average the "LTM-Gauss_v2" and "NFW_v2" Zitrin et al. (2009, 2013) models for μ, adding their 3σ formal errors ($\lesssim$0.05) in quadrature to SSF's (much larger) dispersion to estimate its uncertainty. Identical models are not available, but the "LTM-Gauss_v1" estimate is consistent with SSF's HFF-derived μ at 2.4σ. In all cases, μ is a small correction ($\lesssim$0.3 dex; Table 1), and surface densities/ratios such as sSFR $\equiv$ SFR/M_* are μ-independent.

[14] https://ned.ipac.caltech.edu/forms/calculator.html
[15] https://archive.stsci.edu/prepds/frontier/lensmodels/#magcalc

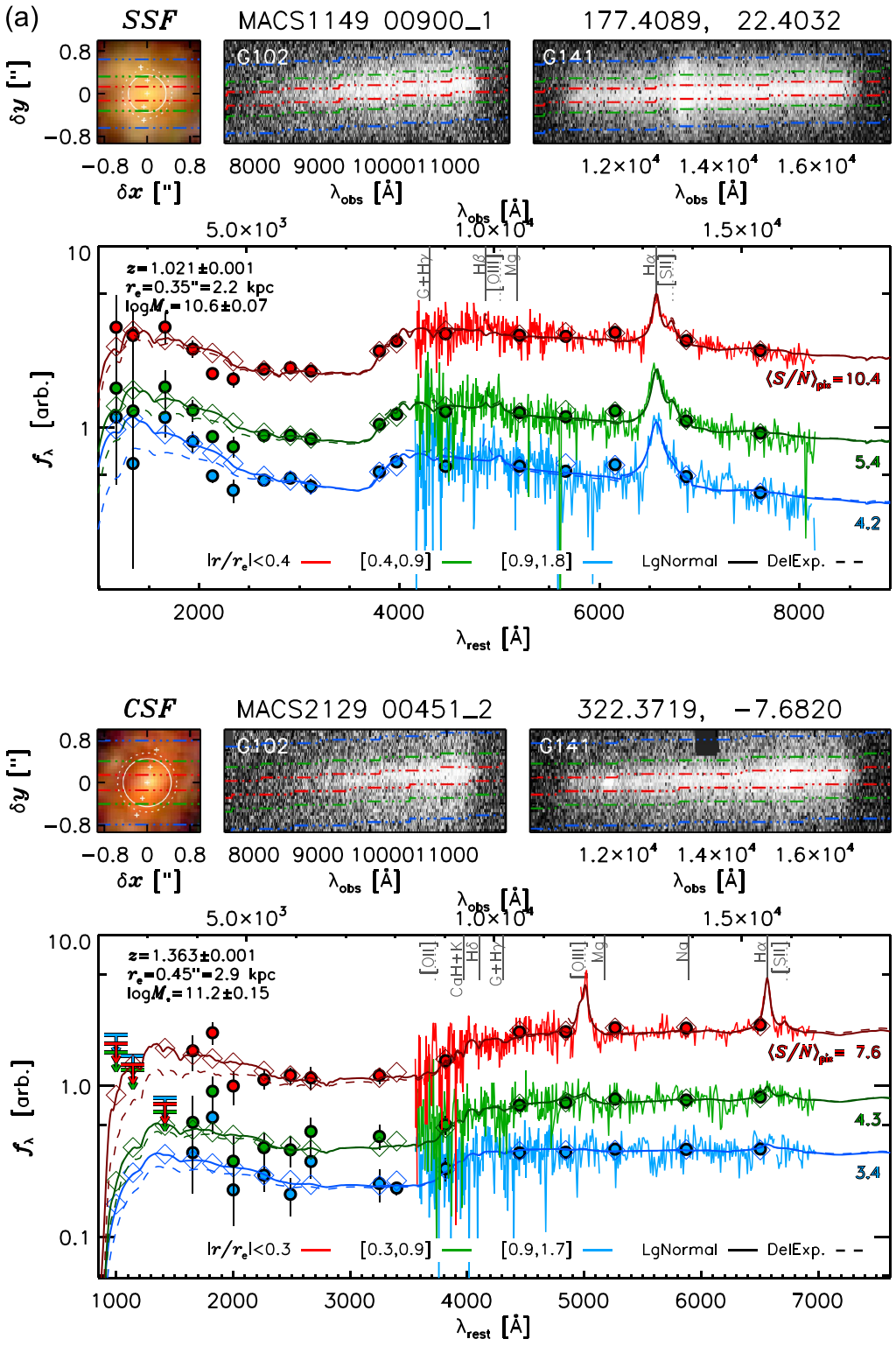

Figure 2. (a) Images, 2D spectra, and spatially resolved 1D extractions for SSF and CSF (others on next page). The top left images are insets of those in Figure 1 showing 1D r_e (solid) and 2D half-light radii (dashed circles), the extraction regions, and the light-weighted (x, y) centroids for each. Rightward of these are the 2D GLASS spectra with extraction zones overplotted in red (INNER), green (MIDDLE), and blue (OUTER). Steps are due to the spectra not being (x, y) rectified. Black areas on the 2D spectra show contamination/missing data masking. The main panel shows corresponding 1D SEDs color-coded by region. The best-fit *pyspecfit* lognormal (delayed exponential) SED fit is plotted as a solid (dashed) line, with open diamonds showing the predicted locations of the photometry. In all but PSB, the lognormal provides as good a fit to the data as the delayed exponential SFH. The radial extent of each extraction zone is listed at the bottom. (b) Images, 2D spectra, and radial 1D spectra for PSB and PAS.

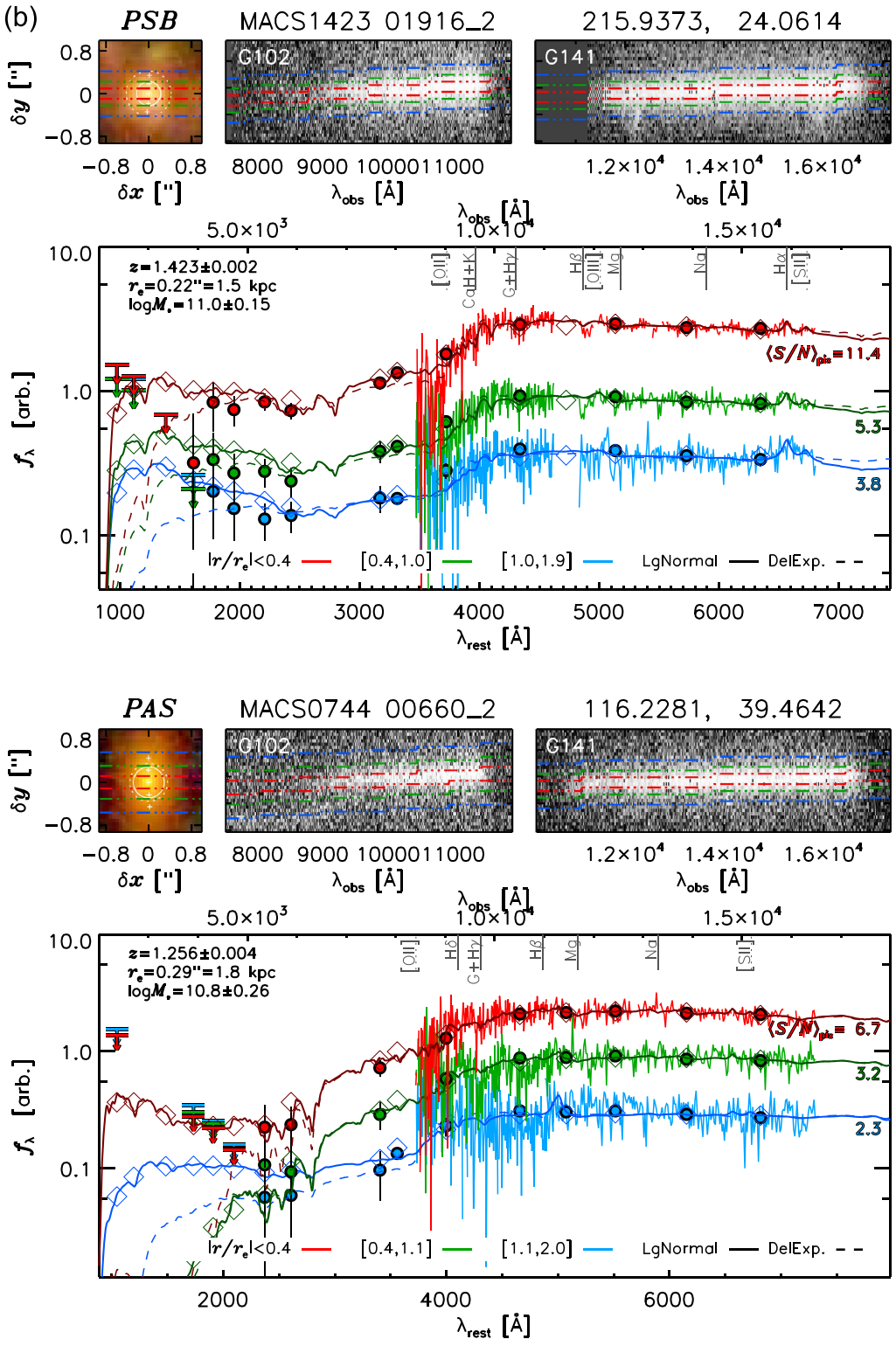

Figure 2. (Continued.)

3. Spectral Synthesis Modeling

We jointly fit each galaxy's optimal, INNER, MIDDLE, and OUTER broadband fluxes and spectra to infer its spatially integrated and resolved M_*, SFR, A_V (marginalized over all other quantities), and SFH. For our main analysis, we adopt the lognormal parameterization of Gladders et al. (2013),

$$\mathrm{SFR}(t) \propto \frac{1}{t\sqrt{2\pi\tau^2}} \exp\left[-\frac{(\ln t - T_0)^2}{2\tau^2}\right], \quad (1)$$

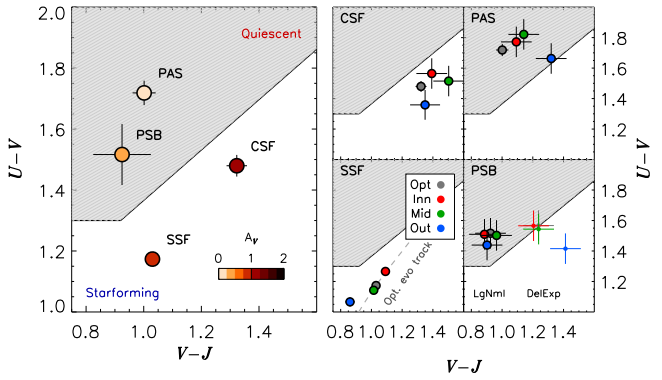

Figure 3. Left: synthetic integrated rest-*UVJ* colors color-coded by A_V. Consistent with appearances, CSF and SSF lie in the star-forming region and are more extinguished than their quiescent counterparts. Right: resolved colors from the radial spectral extractions. CSF and SSF have x or y gradients such that INNER regions are redder than OUTER ones. The quiescent PAS and PSB show opposite or no gradients (with the caveat of PSB's limited radial coverage). SSF's pieces lie roughly along the trajectory of its integrated SED fit, suggesting that larger-r regions developmentally lag INNER ones ("inside-out growth"). PSB is the only system with rest-frame color SFH systematics (both results plotted at bottom right), perhaps due to its truncated history or our lack of rest-J coverage (available only from insufficiently resolved *Spitzer* data).

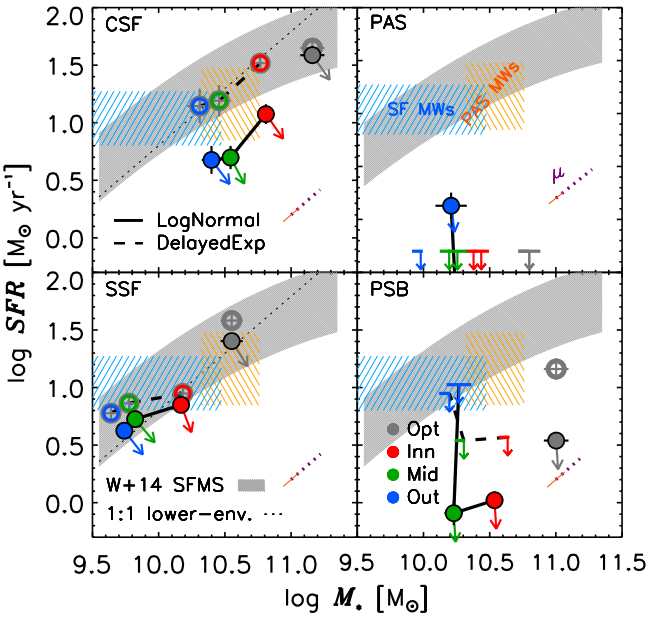

Figure 4. Spatially resolved SFR–M_* plane. Star-forming (passive) systems are plotted at left (right). Filled symbols/solid lines show lognormal results; open symbols/dashes show delayed exponentials. Bars denote 2σ upper limits; arrows are (M_*, SFR)(t) unit vectors averaged over $t_{obs} \pm 1$ Gyr. The $z \sim 1.25$ SFMS (Whitaker et al. 2014) is plotted in gray with blue/orange blocks locating progenitors of $z = 0$ MW-mass SF/passive galaxies (Gladders et al. 2013). Resolved and integrated metrics (colored and gray circles, respectively) support similar inferences with telling exceptions: the SFMS's bend allows galaxies to be on the locus while their components are not (CSF), suggesting that locus-based inferences can bias insights into star formation physics. Dotted purple/thin orange lines show magnification effects/uncertainties.

where T_0 is the SFH's half-mass time (in ln Gyr) and τ sets its width. This form has significant advantages over, e.g., a delayed exponential (e.g., Lee et al. 2010), including a smooth derivative over all t, and better agreement with SFHs from simulations (Ciesla et al. 2017; Diemer et al. 2017). Further, ensembles of lognormals reproduce many observations at $z \lesssim 8$ (Gladders et al. 2013; Abramson et al. 2015, 2016; Dressler et al. 2016). That said, since SFR(t) > 0 for all t, the lognormal cannot be normalized without a priori knowledge of t_{obs}. Hence, we determine a fine redshift solution in a first-pass fit using a delayed exponential SFH, then fix the lognormal fitting to that z. As the resultant delayed exponential SFHs are unphysical (Figure 19), all quantities quoted below reflect lognormal results unless stated otherwise, e.g., when assessing systematics (Section 4.2). Appendices D and E provide relevant delayed exponential-based results.

All fitting is done with *pyspecfit* (Newman et al. 2014), a flexible Bayesian python package wrapped around the *MultiNest* Monte Carlo Markov chain engine (Feroz & Hobson 2008). We assume Bruzual & Charlot (2003) templates, a Salpeter (1955) initial mass function, solar metallicity (Gallazzi et al. 2005, 2014), a Calzetti et al. (2000) dust law, and a χ^2 likelihood (see Newman et al. 2014; Equation (B1)). Appendix B lists other fit parameters/details, which include Hα, Hβ, [O III], and [S II] emission-line equivalent widths.

Thus, SED fitting produces a redshift and 4×2 sets of M_*+SFR+SFH parameters for each galaxy describing the optimal, INNER, MIDDLE, and OUTER extractions. Mass estimates are consistent across SFH choice, though SFRs may not be (Section 4.2). Broad priors are placed on SFH parameters and other outputs (e.g., A_V). Best-fit values are the medians of the *MultiNest* posteriors, with the 16th–84th percentiles as formal uncertainties. We use the full parameter covariances when reconstructing SFH-related confidence envelopes.

4. Results

We now characterize the sample's spatially integrated (Section 4.1) and resolved (Section 4.2) diversity at t_{obs}, then chart its development over multiple epochs (Section 4.3). The temporal projections reveal many signs of inside-out growth, hints of a link between high bulge fractions and nonconstant SFHs, and a difference between longitudinal and cross-sectional size reconstructions (Section 4.3.2), all encouraging further study.

We proceed by analysis level, because this paper's main goal is not to focus on comparing specific, detailed properties of four galaxies but rather to illustrate how data can be used to bridge the gap from cross-sectional, spatially integrated inferences to more longitudinal, spatially resolved ones much closer to modern models. We thank our readers for their indulgence.

All quantities are magnification-corrected and incorporate that uncertainty.

4.1. Integrated Properties at t_{obs}

4.1.1. Masses and Star Formation Classes

Table 2 lists each galaxy's monolithic properties. Spanning $10.5 \lesssim \log M_* \lesssim 11.2$, they are all likely progenitors of modern MW to $\gtrsim$M31-mass galaxies (see below).

Figure 1 shows the sample's integrated spectrophotometry. Here IDs 00451_2 and 00900_1 show notable Hα/UV flux and prominent disks/blue spiral arms. The other two sources, IDs 00660_2 and 01916_2, show either no or much less Hα/UV

flux and spheroidal, redder appearances. These sources' *UVJ* (Williams et al. 2009) and SFR–M_* locations (Figures 3 (left) and 4, respectively) reflect these statements, with 00451_2 and 00900_1 lying outside the quiescent box and on the $z \sim 1.25$ star formation "main sequence" (SFMS; Noeske et al. 2007; Whitaker et al. 2014) and 00660_2 and 01916_2 lying in the box and off the SFMS. Hence, the sample is split equally into two star-forming and two passive galaxies.

However, Figure 1's spectra reveal more diversity. First, despite both being "normal" SFMS galaxies, 00451_2 is redder/has a shallower UV slope than 00900_1, suggesting it is more mature (Section 4.3). This is consistent with 00451_2's $\sim$4$\times$ greater mass and reduced EW(Hα+[N II]) ($\sim$sSFR) and the fact that its resolved components actually lie off the SFMS (Section 4.2; the locus's bend keeps it defined as "star-forming"). Hence, we refer to these star-forming systems as

1. 00451_2 $\equiv$ "CSF"—continuously star-forming
2. 00900_1 $\equiv$ "SSF"—strongly star-forming.

Notable [O III] emission suggests that CSF hosts an AGN, confirmed by its resolved spectra and mass–excitation diagram (Juneau et al. 2014; Figures 2 and 6).

The two passive galaxies are also distinct: 00660_2 is unquestionably old, with a red continuum, essentially no UV flux, and strong G-band absorption. Meanwhile, 01916_2's bluer, A-star-like spectrum (Figures 3 and 8); higher UV flux; and residual Hα+[N II] emission, as well as its photometry's preference for the rapidly decaying delayed exponential SFH (Section 4.2), suggest that it was rapidly quenched within $\sim$1 Gyr of $t_{\rm obs}$ (Dressler & Gunn 1983; Poggianti et al. 1999). We therefore refer to the quiescent systems as

1. 00660_2 $\equiv$ "PAS"—passive
2. 01916_2 $\equiv$ "PSB"—post-starburst.

From Figure 4, SSF and PAS appear set to become $\sim$MW-mass $z = 0$ E/S0s, while CSF and PSB are modern $\gtrsim$M31-mass progenitors. Given their aforementioned spectral diversity, dissecting these galaxies in space and time thus provides insights relevant to—if not representative of—important parts of parameter space (see also Section 5.1.3).

Note that we use SFH-based SFR inferences at all t. This (1) ensures consistency with evolutionary mass projections; (2) captures more representative mass growth rates (H II regions vary on $\sim$0.1 Gyr timescales); (3) avoids line flux and dust correction biases due to Hα+[N II] and Hβ+[O III] blending (but see Wang et al. 2017); and (4) reduces AGN ambiguities (present in CSF). Nevertheless, using dust-uncorrected EW(Hα +[N II]) as an sSFR proxy yields similar trends to those inferred from full SED fitting (Appendix E, Figure 20).

4.1.2. Size and Structure

Figure 5 (left) shows the sample on the size–mass plane. From their 2D half-light radii ($\sim$2.1–3.6 kpc), the passive PAS and PSB lie where they are expected to, while the star-forming galaxies are small for their mass (van der Wel et al. 2014; we plot SExtractor estimates). Trends hold in 1D ($r_e \sim 1.5$–3.0 kpc), except PSB shrinks notably (likely due to further compressing what is already a highly concentrated light profile; see next paragraph). Small galaxies' narrower spectra are less likely to be contaminated, so this could be a selection effect or due to chance.

Structure should also encode evolutionary physics. Figure 5 (right) shows the sample's mass–mass concentration—M_*

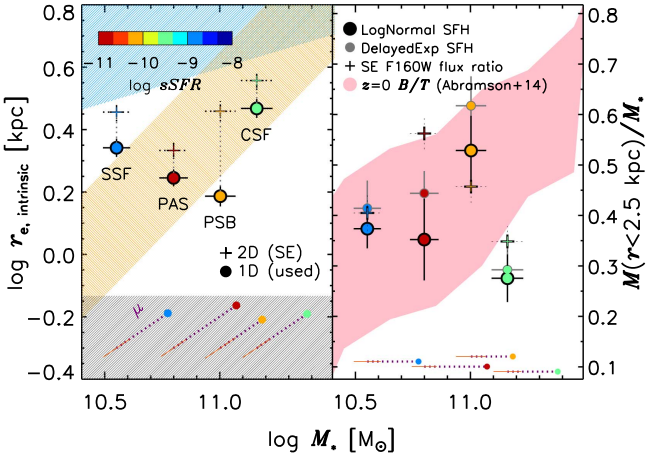

Figure 5. Left: the size–mass plane. Points are color-coded by sSFR with circles and crosses showing 1D r_e used in this analysis and 2D SExtractor half-light radii, respectively. Blue and orange shading shows van der Wel et al. (2014)'s star-forming and passive $z = 1.25$ relations, with the *HST* resolution limit in black. Right: the $M_*(r < 2.5$ kpc) fraction ($\sim B/T$)–mass plane with Abramson et al. (2014)'s $z = 0$, 25%–75% range shaded pink (a good description at $z \lesssim 2$; Lang et al. 2014). Gray circles and dotted crosses show delayed exponential SFH and single-band SExtractor estimates to provide a sense of systematics. All galaxies have normal B/T for their mass except CSF, which is unexpectedly disk-dominated.

($r \leqslant 2.5$ kpc)$/M_*$ relation. To the extent that this quantity reflects bulge-to-total ratios, the systems span $B/T \sim 30\%$–60%, placing most on the $z = 0$–2 expectation (Abramson et al. 2014; Lang et al. 2014; latter plotted). Perhaps revealingly, however, CSF is in the lower quartile for its mass (Section 5.1).

We calculate mass concentrations by interpolating each zone's stellar mass surface density ($\Sigma_{M_*}(r)$) onto a finer grid, assuming circular symmetry, and integrating to $2\,r_e$, e.g., $M_{*,\rm int}(<r) = 2\pi \int_0^r r'\,\Sigma_{M_*}(r')dr'$. We force $M_{*,\rm int}(<2\,r_e)$ to match the optimal extraction M_* estimates. While not formally self-consistent, this process can be repeated as we evolve the galaxies through time to estimate half-mass radii and "B/T" trajectories in a way comparable to cross-sectional studies (Morishita et al. 2015). Before renormalizing, total masses for CSF and PAS are consistent, with the others $\sim$0.3–0.4 dex lower, perhaps due to their clumpier structure. The SFH systematics are $\Delta B/T \sim 0.1$, similar to offsets assuming B/T is the ratio of F160W flux at $r < 2.5$ kpc to SExtractor's `FLUX_AUTO`. So, in sum, the robust interpretation of Figure 5 (right) is that these galaxies have normal B/T for their mass except for CSF, which is unexpectedly disky.

4.2. Spatially Resolved Properties at t_{obs}: Colors, Mass and SFR Densities, and Dust

With the sample globally situated as a set of four mainly unexceptional passive and star-forming MW- and M31-mass progenitors, we now resolve its properties spatially at $t_{\rm obs}$.

Figure 3 (right) shows color gradients in $U - V$, $V - J$, or both in the star-forming systems CSF and SSF, such that INNER regions are at least redder than OUTER ones. As we will soon find, these trends are due to each zone's intrinsic stellar populations, not dust. This is expected—bulges are old—but it is interesting that SSF's colors fall roughly along the evolutionary trajectory of a single lognormal SFH (dashed

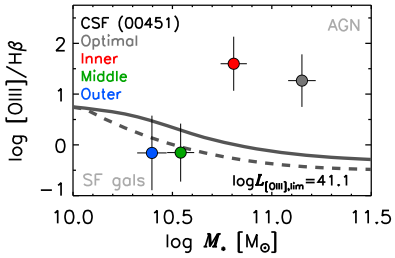

Figure 6. CSF's resolved mass–excitation diagram (Juneau et al. 2014) at GLASS's 2σ $F_{\rm lim} \simeq 2 \times 10^{-17}$ erg s^{-1} cm^{-2} (Schmidt et al. 2014; i.e., $\log(L_{[\rm O\ III]}/{\rm erg\ s^{-1}})_{\rm lim} = 41.1$). INNER/optimal estimates imply AGN activity (above the solid line). Meanwhile, the MIDDLE and OUTER regions lie with normal star-forming galaxies (below the dashed line). These maintain a combined SFR $\sim$ 10–25 $M_\odot$ yr^{-1}, apparently unquenched by the AGN (Figure 4).

line), with its MIDDLE and OUTER regions simply lagging INNER by some delay. We revisit this signal below.

The passive systems, PAS and PSB, are either uniformly red or have gradients in the opposite sense, reddening with increasing r at least in $V - J$. This may be due to dust or reflect SFH systematics. The latter are significant in PSB: because delayed exponentials can fall faster than lognormals, better mimicking what in reality may be a discontinuity, these models fit PSB's UV photometry better at all r (Figure 2). Rest-J SED data would likely reduce this tension but will not be available at sufficient spatial resolution until *JWST*. Regardless, the exponential UV fit quality and lognormal color inferences agree in implying that whatever quenched PSB acted quasi-globally, such that much of the galaxy—at least out to its 2D half-light radius—shut down at about the same time.

While PSB's SFH truncation was spatially extended, Figure 2's radially resolved spectra conversely reveal that CSF's MIDDLE and OUTER SFRs remain $\sim$3–6 $M_\odot$ yr^{-1} despite apparent AGN activity (Figures 1 and 6). That said, these SFRs are below average for objects with CSF's INNER, MIDDLE, or OUTER regions' masses. Indeed, these components lie 1.5–2σ below the SFMS, even though CSF as a whole appears normal (Figure 4). This is due to the SFMS's bend at log $M_* \gtrsim 10$ (e.g., Salim et al. 2007; Whitaker et al. 2012, 2014; Abramson et al. 2014; Schreiber et al. 2016) and affects the bluer SSF to a lesser extent. This phenomenon—and similar but opposite effects in the $z \approx 0$ "Green Valley" (Dressler & Abramson 2015; Vulcani et al. 2015a)—highlights key complications in inferring physics from the SFMS: it is hard to see how CSF could be star-forming while its pieces are quenched. As with emission-line ratios (Sanders et al. 2017), integrated inferences are not always the sum of their parts, a dichotomy only understandable using spatially resolved data.

Figure 7 quantifies other radially resolved sample trends. The top row shows galaxy surface mass density profiles: $\Sigma_{M_*}(r) \equiv M_*(r)/{\rm Area}(r)$, where Area($r$) is based on the number of $0\farcs065 \times 0\farcs065$ pixels in the SExtractor segmentation map in each radial zone. The left panel shows Σ_{M_*} in absolute units, and the right panel is normalized to inner 1 kpc means. Interestingly, the star-forming CSF and SSF have steeper Σ_{M_*} profiles compared to their passive counterparts (though SSF is the least dense system). This remains true, if less significant, when viewed in terms of physical radii instead of r/r_e (Figure 20) and suggests that either (1) the passive systems have already undergone some amount of, e.g., minor merger–driven envelope building (e.g., Newman et al. 2012; Nipoti et al. 2012; Morishita & Ichikawa 2016) or (2) the star-forming

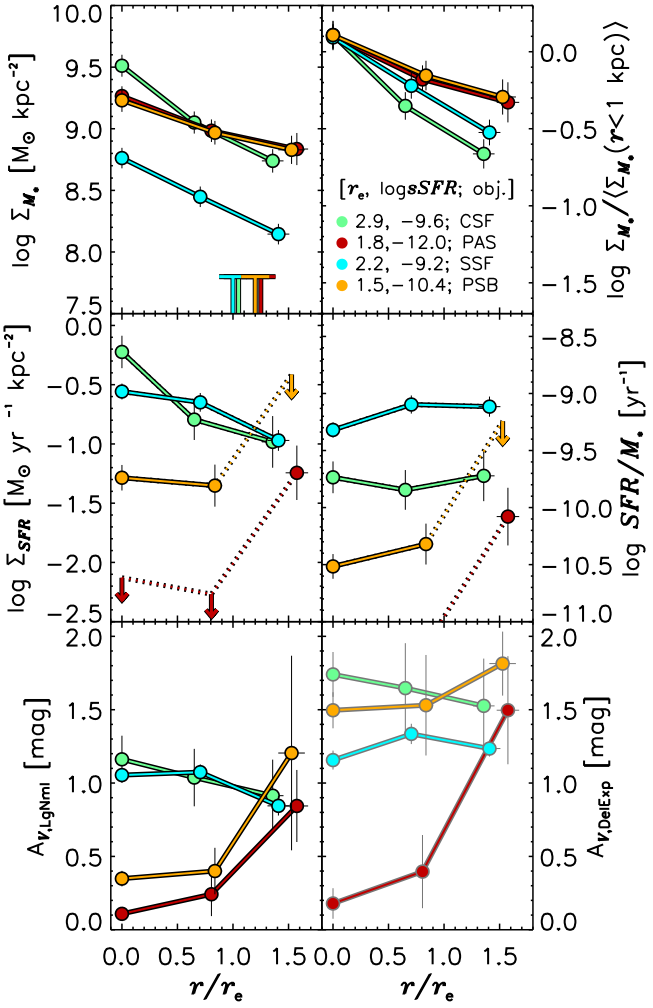

Figure 7. Top: lognormal absolute (left) and relative (right) mass surface density profiles. The latter are normalized to each source's central kpc mean. Middle: SFR surface density and sSFR profiles (areas cancel). Bottom: A_V profiles from lognormal (left) and delayed exponential (right) SFHs. The sSFR (r) values of the star-forming systems differ by $\sim$4×, but they have consistent $\Sigma_{\rm SFR}$ at all r, favoring gas surface density over mass as an SFR governor. Here A_V exhibits SFH systematics, pointing to it as a test of SFH models (though the rest-UV S/N is low in the passive systems). Bin x offsets reflect pixelation.

systems are growing "inside-out," with their disks following their bulges (e.g., Eggen et al. 1962; Silk & Norman 1981; Kepner 1999; Tacchella et al. 2015).

Figure 7 (middle) provides some leverage on the latter issue. Here we plot SFR surface density—$\Sigma_{\rm SFR}(r) \equiv {\rm SFR}(r)/{\rm Area}(r)$ (left)—and sSFR gradients (right). Here CSF exhibits a fairly constant sSFR(r), while SSF's rises by $\sim$40%–80% with increasing r; i.e., its center is perhaps half as active as its disk (see also Nelson et al. 2016a; Abdurro'uf & Akiyama 2017). With its *UVJ* color gradient, this finding again suggests that SSF's bulge is relatively developmentally advanced. On the other hand, CSF's uniform lower sSFR(r) suggests that its higher mass was built up more gradually at all r (Section 4.3.2). These star-forming galaxies therefore had quite different pasts.

Nonetheless, CSF and SSF do share a trait: while their OUTER sSFRs differ by $\gtrsim$3×, they correspond to precisely the same SFR surface density—$\Sigma_{\rm SFR}/M_\odot\ {\rm kpc}^{-2} \simeq 0.1$—and indeed nearly identical SFRs (Figure 4). Taken together, Figure 7's middle panels thus imply that quantities beyond stellar mass are important to characterizing or controlling star

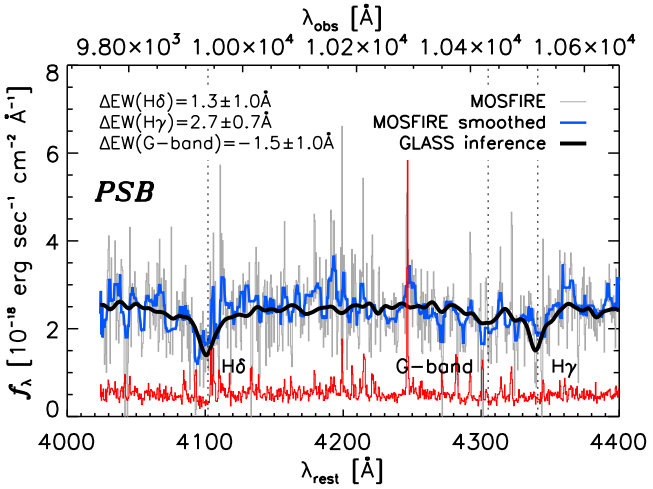

Figure 8. PSB's optimal lognormal model spectrum (black; broadened to $\sigma_v = 190 \pm 40$ km s^{-1}) compared to MOSFIRE data (gray). Red shows rms errors, and blue shows median-smoothed data (10 Å window). Implied line strengths show that the lognormal SFH may reproduce these high spectral resolution data better than the delayed exponential, though the latter better matches PSB's UV fluxes (cf. Table 3 and Figure 2).

formation in star-forming galaxies; CSF's relatively heavy disk supports the same absolute level of star formation as SSF's lighter yet similarly sized disk. Without resolved data, this phenomenon would not have been detected.

This signal—where sSFR but not $\Sigma_{\rm SFR}$ declines at fixed r with increasing mass—is not inconsistent with Nelson et al. (2016a)'s stacked *HST* Hα maps (see their Figures 12 and 13), though sample size prevents us from saying more.

Note that the apparent upturns in PAS's and PSB's OUTER $\Sigma_{\rm SFR}$ and sSFR may reflect the fact that these inferences are constrained mainly by upper limits in the rest-UV photometry. Along with A_V (see below), they may therefore be unreliable. Certainly, we do not place too much weight on them.

Finally, Figure 7 (bottom left) shows lognormal-derived $A_V(r)$. The higher dust content inferred globally for CSF and SSF holds at all r probed, in qualitative agreement with gas-phase Balmer decrement estimates by Nelson et al. (2016b), or perhaps the flatter trends inferred by Tacchella et al. (2016a). On the other hand, PAS appears clear of dust at $r \lesssim r_e$ but has comparable $A_V \sim 1$ mag to the star-forming galaxies at $\sim$1.5 r_e. If not a reflection of low photometric S/N, this could be a hint of ancient spiral arms and thus a sign of inside-out growth/quenching or the contents of recently accreted satellites. While opposite to the A_V trend inferred for a more massive $z \sim 2.15$ system by Toft et al. (2017), this scenario is consistent with those authors' sSFR inferences.

PSB is edifying in this regard if we bring in Figure 7 (bottom right), showing A_V trends derived using delayed exponential SFHs (Section 3). There, PSB goes from having a $\sim$dust-free, PAS-like center to $\sim$1 mag more extinction at all r, similar to the star-forming galaxies, which are also elevated. These effects are due to SFH geometry: the exponential's delay causes that model to use less than the available time to produce a given M_*. Hence, its mean SFR is higher than a lognormal's —which starts at $t = 0$—naturally leading to higher SFR($t_{\rm obs}$) (Figure 4). Despite the higher SFRs, however, the exponential models cannot overshoot the UV photometry, so the fitter adds dust to diminish UV but not optical/infrared (OIR) flux, elevating A_V for systems with even trace recent star formation.

Table 3
ID 01916_2 (PSB) GLASS/MOSFIRE Spectral Indices

Feature[a]	$EW^{\rm Del.\ Exp.}_{\rm GLASS\ inf}$ (Å)	$EW^{\rm Lognormal}_{\rm GLASS\ inf}$ (Å)	$EW_{\rm MOSFIRE}$ (Å)[b]
Hδ_A	9.3	7.4	5.3 ± 1.1
Hδ_F	6.4	5.1	4.7 ± 0.8
Hγ_A	6.2	4.8	1.2 ± 1.0
Hγ_F	4.8	4.5	2.7 ± 0.7
G4300	−0.5	1.2	2.7 ± 1.1
χ^2/ν[c]	2.12	1.95	...

Notes.
[a] Lick definition (astro.wsu.edu/worthey/html/index.table.html).
[b] Bootstrapped uncertainties.
[c] $\nu = 835$. Spectra in Figure 8.

Table 4
Delayed Exponential-derived Integrated Properties

Tag	log $M_*/M_\odot$ [a,b]	log SFR/$M_\odot$ yr^{-1} [a,b]	A_V (mag)
PAS	10.77 ± 0.07 (0.10)	<-9.13[c]	0.25 ± 0.13
SSF	10.54 ± 0.06 (0.09)	1.58 ± 0.06 (0.07)	1.31 ± 0.03
PSB	11.05 ± 0.07 (0.10)	1.16 ± 0.15 (0.27)	1.50 ± 0.09
CSF	11.17 ± 0.07 (0.16)	1.65 ± 0.14 (0.20)	1.28 ± 0.14

Notes.
[a] Quadrature sum of INNER + 2 MIDDLE + 2 OUTER M_* and SFR errors in parentheses; M_* are consistent with lognormal estimates.
[b] Magnification-corrected (Table 1); uncertainties incorporate μ errors.
[c] Formal 2σ limit.

As to which model is "right," a MOSFIRE *Y*-band spectrum for PSB was independently obtained as a slit-mask filler (PI: Bradač; 2017 April 27) covering $\lambda_{\rm rest} = 4000$–4400 Å, a region containing three age-sensitive spectral features: Hδ, Hγ, and the *G* band. Figure 8 shows that this spectrum's much higher resolution features are indeed well predicted by the fit to the low-resolution *HST* spectrophotometry. Quantitatively, comparing these data to the delayed exponential and lognormal SFH-inferred templates yields somewhat better agreement in these lines' equivalent widths with the lognormal (Table 3), spectroscopic evidence that that model is a decent description of PSB's actual history even if it falls too slowly to match the system's rest-UV flux. Indeed, the observed Balmer equivalent widths are smaller—and *G* band larger—than either model would predict, suggesting an older stellar population (though Hγ especially may suffer infilling from residual emission). Note that since equivalent widths are flux ratios, absent radical asymmetries, they are insensitive to slit losses.

4.3. Spatiotemporally Resolved Properties: Data "Longitudinalization"

Section 4.2 resolved the galaxies in space, taking them from point-like (M_*, SFR, A_V) to distribution-like descriptions (Σ_{M_*}, $\Sigma_{\rm SFR}$, A_V)(r). This showed that systems with different sSFR(r) can have similar $\Sigma_{\rm SFR}(r)$, galaxies can lie on the SFMS while their resolved components do not, and significant SFRs can persist at large r despite AGN activity.

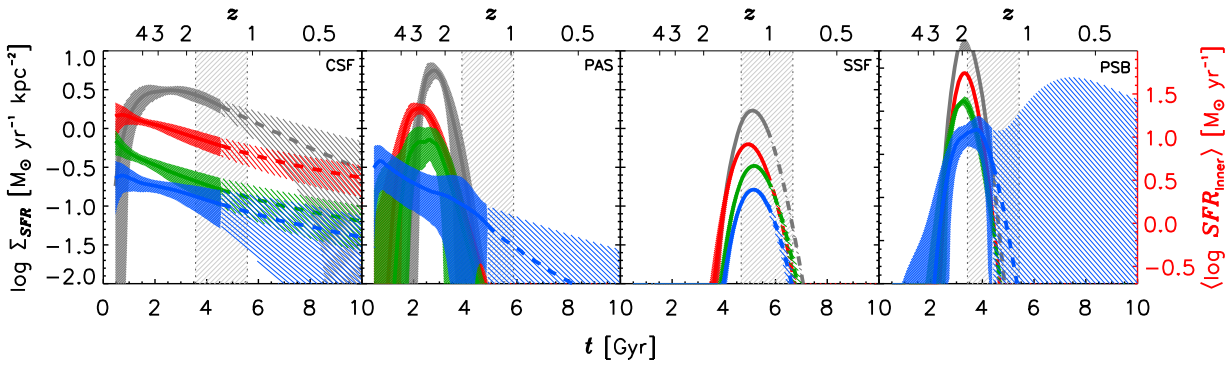

Figure 9. Spatially integrated and resolved SFHs. Colors correspond to previous figures with optimal extraction results (scaled to INNER surface areas) in gray. Epochs before t_{obs} are shown as solid lines; forecasts are dashes. Vertical bands show the $t_{obs} \pm 1$ Gyr interval over which we draw longitudinal inferences (Figure 10). Envelopes show 16th–84th percentile spreads in SFR(t) from the (T_0, τ) *pyspecfit* covariances. All galaxies are observed after their peak, and all but CSF show signs of inside-out/bulge-first growth. INNER SFRs approach/are exceeded by MIDDLE and OUTER SFRs between t_{peak} and t_{obs}. Conversely, the relatively disky CSF (Figure 5) had an ∼constant SFH across its face. SSF is growing strong—proportionately more so at larger r (Figures 3 and 4)—and PAS has been quenching for ∼twice as long as PSB. The right y-axis shows the absolute SFR_{INNER} at the sample's mean area and magnification for reference.

Such facts increase the burden on models aiming to describe these galaxies at t_{obs}, but validating their causal implications requires more input: empirical inferences about how these specific systems—not the galaxy population—evolved. We present a suite of such temporally resolved inferences here to constrain what the sample most likely did and will look like.

4.3.1. Spatially Resolved SFHs

Figure 9 shows the sample's spatially integrated and resolved lognormal SFHs. As suggested in Section 4.1, these show that CSF continuously formed stars at a relatively constant rate across its face, declining by only ∼3× since its SFH peaked at $z > 4$. It is thus much more mature than SSF, which is within ∼1 Gyr of peak activity. A similar story holds for the passive systems: PAS has been "quenching" for perhaps twice as long as PSB, though both are now farther from their peak/have faster-falling SFRs than their star-forming peers. All four systems are in the declining phase of their lives, but this was not true of their $z \sim 2$ progenitors. Except for SSF—which has grown substantially since that epoch—those objects would be within a factor of ∼2 of their current mass but at their maximal SFRs. Section 4.3.2 elaborates on this point.

More resolved trends are shared by the three nonconstant SFH systems: compared to peak, observed SFRs in the INNER regions of SSF, PAS, and PSB are closer to or below their MIDDLE and OUTER values. This is the formal signature of inside-out growth and is consistent with these systems' locations in Figure 5, where they have significantly higher B/T than the constantly star-forming CSF. Section 5 focuses on the connection between these observations.

4.3.2. Size and Structural Evolution

Figure 10 presents reconstructions of the mass profile evolution of the sample galaxies derived from the spatially resolved SFHs. Each row shows results for one galaxy in order of decreasing $sSFR_{obs}$ (SSF to PAS). From left, the panels show (1) Σ_{SFR} versus Σ_{M_*} in each radial zone; (2) Σ_{SFR} versus time in each zone; (3) $\Sigma_{M_*}(r; t)$ profiles at $t_{obs} \pm 1$ Gyr relative to observed INNER values (profile shape evolution); and (4) $\Sigma_{M_*}(r; t)/\Sigma_{M_*}(r; t_{obs})$ (total mass growth) at the same intervals (where we are willing to extrapolate the SFHs). Points in the left panels mark the epochs in the right panels.

Starting at right, all galaxies except PAS are inferred to have gained significant M_* at all r in the Gyr preceding t_{obs}. Further—clearest in SSF—the two star-forming systems should grow marginally in the subsequent Gyr ($\lesssim$25%). The inside-out/bulge-first growth of SSF is again obvious here: proportionately, OUTER regions gain more mass in this 2 Gyr period than INNER ones (∼0.8 versus ∼0.6 dex). Hints of this trend appear in PSB, but limited radial coverage contributes to large uncertainties there. The second left panel, showing Figure 9's SFHs zoomed to the $t_{obs} \pm 1$ Gyr window, highlights how exceptional CSF is in this regard: its resolved SFHs never cross but maintain rank ordering over all time.

The leftmost panels of Figure 10 reinterpret these signals by replacing time with Σ_{M_*} on the abscissa. From this perspective, the inside-out growth signature is expressed as inside-out quenching; what is a gradual decline in SFRs with time transforms into an abrupt event as galaxies—again, with the notable exception of CSF—appear to hit a Σ_{M_*} wall at all r, with INNER regions doing so well before OUTER ones. At root, this phenomenon—the "L-shaped track" of Barro et al. (2017a)—is a reflection of each zone's monotonically declining sSFRs, leading to asymptotic final masses. Using logarithmic x-axes (as we do here) emphasizes this mathematical effect and de-emphasizes meaningful if undramatic linear M_* increases. Indeed, CSF's aforementioned "modest" 25% future growth amounts to $\sim 2 \times 10^{10}\, M_\odot$.

This highlights a distinction between "activity" as defined by future fractional mass growth (systems that can at least double their M_* in a Gyr) versus current star formation: if the former is used, then even galaxies making tens of $M_\odot$ of stars per year are arguably quenched, with "active" galaxies being only those with sustained high sSFRs; i.e., rising SFHs. The point spacings on the curves in Figure 10 (left) clearly illustrate this statement: SSF's OUTER region grew by nearly 10× in M_* over the 2 Gyr ($\sim 0.4\, t_{Hubble}$) probed, contrasted with CSF's $\lesssim$2× OUTER growth despite its higher mean SFR (Figure 17).

So, taken together, the two left panels of Figure 10 thus explain how the question of why SFHs stop rising (in time) can be readily reinterpreted as what (about mass) quenches star formation. Given the vast quenching literature—and Kelson et al. (2016)'s explicit mathematical linking of these two interpretations—we need not dwell on it here. However, features in these data may prove useful to that discussion, such as CSF's apparent contradiction of the idea that Σ_{M_*} is the more

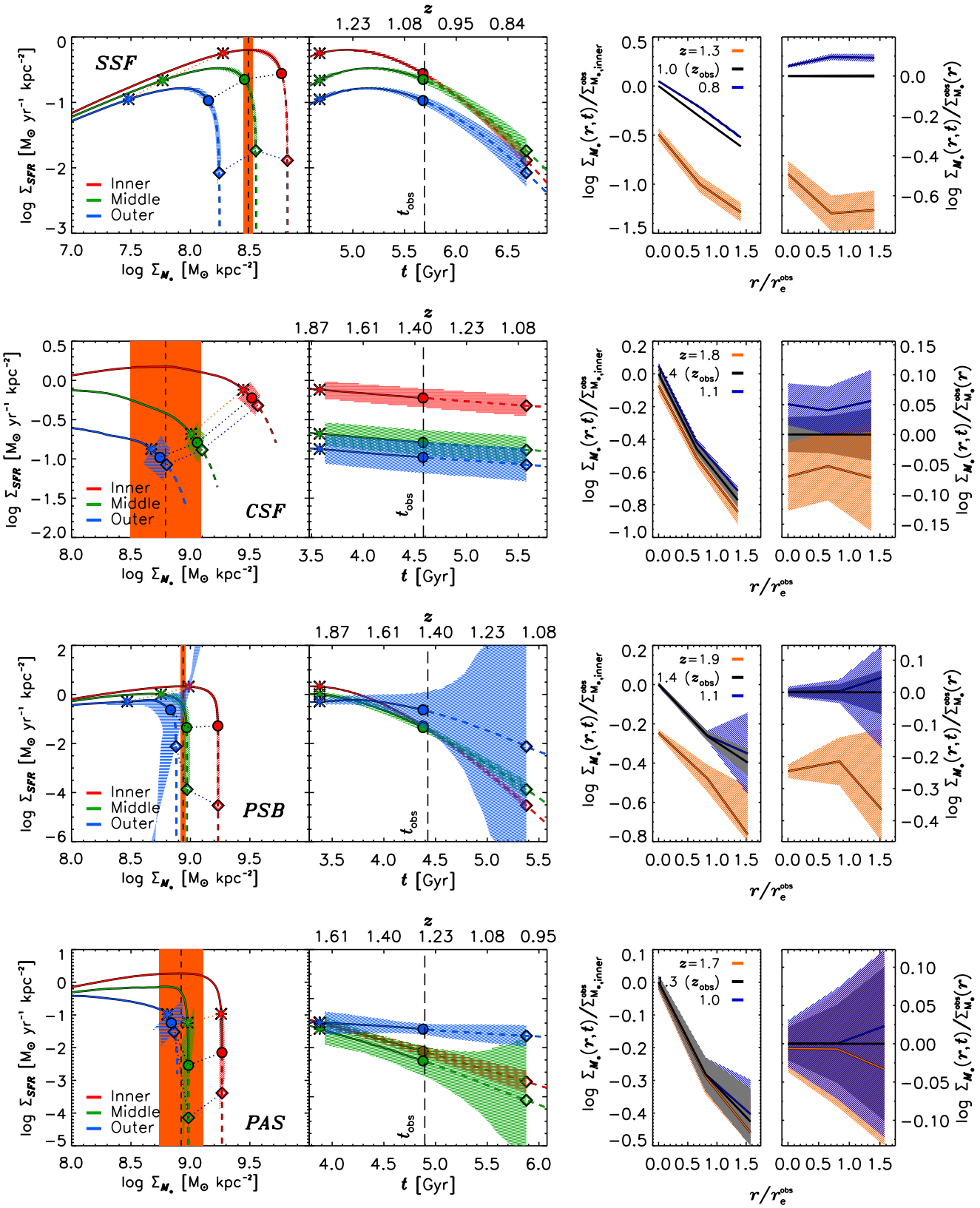

Figure 10. Resolved mass growth histories. From left: (1) $\Sigma_{\rm SFR}(r)$ vs. M_* surface density; (2) $\Sigma_{\rm SFR}(r)$ vs. cosmic time; (3) $\Sigma_{M_*}(r)$ profiles at $t_{\rm obs} \pm 1$ Gyr normalized to INNER values at $t_{\rm obs}$ (shape evolution); and (4) $\Sigma_{M_*}(r)$ at the same epochs normalized to the observed profile (total M_* growth). Points in the left two panels denote epochs in the right two; orange vertical bars show INNER Σ_{M_*} at the time of peak INNER SFR. Shading shows 1σ ranges in all cases. All but CSF show signs of bulge-first growth, visible in the resolved $\Sigma_{\rm SFR}(t)$, the change in rank ordering of $\Sigma_{\rm SFR}(M_*; t)$, and the profile evolution itself. All but CSF (Section 5.1) suggest that INNER Σ_{M_*} at peak SFR is a kind of asymptote for the MIDDLE and OUTER regions, though the INNER regions themselves may ∼double since passing this mark. This trend may reflect a bulge-building–quenching association (Zolotov et al. 2015; Tacchella et al. 2016b; Figure 12, below) or a coincidence given the masses/mass profiles of these systems. Note that the confidence intervals at left reflect the fact that $x = \int y$, so (large) SFR errors propagate to mass.

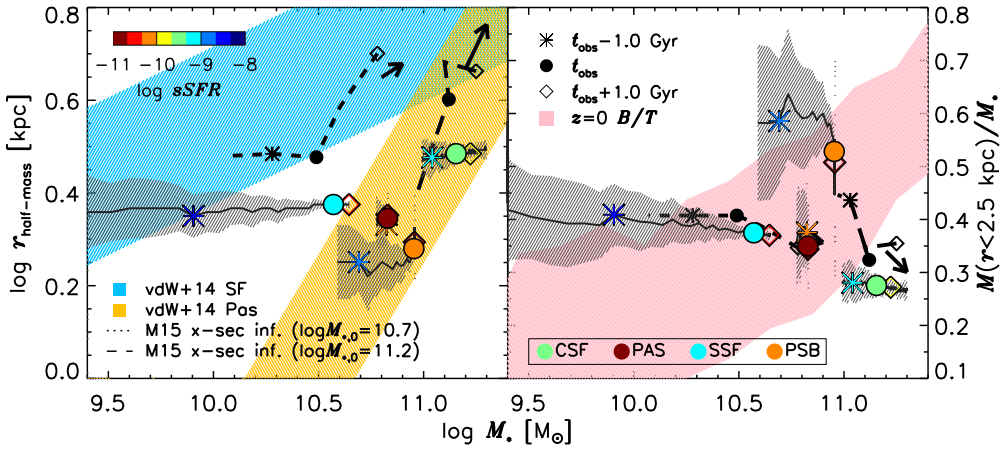

Figure 11. Same as Figure 5 but showing the longitudinally reconstructed half-mass–radius (left) and mass-concentration/B/T–mass evolutionary trajectories of the sample galaxies. Black shading shows 1σ envelopes across $2 \geqslant z \geqslant 0.5$, with points denoting 1 Gyr before (asterisks) and after (diamonds) $t_{\rm obs}$ (filled circles). Point colors show sSFR(t) at the corresponding epochs. Short and long black dashes, respectively, show Morishita et al. (2015)'s cross-sectionally inferred trajectories for galaxies with the space densities of modern MW- and $\gtrsim$ M31-mass systems over the same z-range, highlighting the same intervals (referenced to $\langle z \rangle = 1.27$); arrows denote their time-averaged vectors. Population loci are shaded as in Figure 5. SSF, CSF, and PSB have all grown significantly in M_* since $z = 2$, but not necessarily in size (cf. Genel et al. 2018). This behavior differs from cross-sectional inferences—even for CSF, whose mass evolution is well captured—but B/T inferences are more consistent, with galaxies tending to descend onto the fixed population locus with time from earlier states of relatively high B/T (inside-out growth). At left, note that three systems will end up as small red galaxies at $z \sim 0.5$, though these will have gotten there in very different ways (Section 4.3.2), highlighting the importance of path dependence/temporal diversity underlying single-epoch parameter projections in galaxy evolution.

causally informative abscissa (see Section 5.1). The sample's most massive system, it also has the highest SFR, the same $\Sigma_{\rm SFR}$ as SSF, a system with $\sim$3$\times$ higher sSFR$_{\rm obs}$, and has grown more since its SFH peaked (orange bands). Hence, Σ_{M_*} may not shape galaxy SFHs so much as graphically emphasize whatever does (Bell et al. 2012; Lilly & Carollo 2016).

The final inference we draw from the resolved SFHs is how the sample moved in the size– and B/T–mass planes introduced in Figure 5. Figure 11 plots these projections. Both panels show each system's 1σ trajectory envelopes at $z = 0.5$–2. These are reconstructed by integrating the azimuthally converted $\Sigma_{M_*}(r)$ at each timestep as inferred from the radially resolved SFHs (Section 4.1.2). Here "B/T" is again taken as the mass within $r = 2.5$ kpc over the system's total M_* at any epoch, but sizes are half-mass radii as opposed to r_e (they barely differ at $t_{\rm obs}$). Point styles show $t_{\rm obs} \pm 1$ Gyr as in Figure 10.

Three findings emerge. First, despite growing by $\sim$2.5–10$\times$ in M_*, no galaxy evolved significantly in size or B/T since at least $z = 2$, assuming all evolution is due to in situ star formation. Second, these (flat-ish) trajectories do not follow the galaxy population loci at any of those epochs, or indeed inferences based on fixed 2D or 3D density ($r \propto \sqrt{M_*}$ or $\sqrt[3]{M_*}$) or velocity dispersion ($r \propto M_*$). Third, at least in this sample, and assuming in situ growth, longitudinal size trajectories diverge markedly from abundance-matched cross-sectional inferences (Morishita et al. 2015). Intriguingly though, B/T tracks are more similar, at least for SSF. The mass growth of CSF ($\dot{x}$) is also remarkably well predicted. Section 5.1.3 elaborates.

Our radial resolution and the fact that we must convert chordal (section-based) into radial (annulus-based) densities are important caveats in this context (Sections 4.3.3, 5.2). Yet, assuming we are not grossly in error—we at least predict these galaxies to have reasonable (r, M_*, sSFR) at $z \sim 0.5$—these inferences support a few robust statements.

Regarding motion with respect to loci, echoing results in SFR–M_* (cf. Peng et al. 2010; Speagle et al. 2014; Abramson et al. 2016), even small regions in size–mass space clearly contain galaxies that got there in very different ways. For example, at $z \sim 0.7$, three systems will appear as relatively small red galaxies (absent merging). Yet PAS will have been there since $z \sim 2$, when PSB was a similarly small but high-sSFR "blue nugget," and SSF was an average, much lower-mass star-forming galaxy. Also, if anything, CSF will have traversed across the red (or parallel to but $\sim 2\sigma$ below the blue) galaxy locus since $z \sim 2$, not along it, as suggested by cross-sectional inferences. This highlights the temporal diversity underlying single-epoch parameter projections in galaxy evolution.

That said, knowledge of B/T and sSFR seems capable of breaking some of the above degeneracies. Consistent with the blue-nugget interpretation (Barro et al. 2013, 2016), PSB should have come from a substantially (if not abnormally) bulge-dominated $z \sim 2$ progenitor, whereas SSF's progenitor was much diskier (if still more bulge-dominated than most similar-mass galaxies). (Despite the limited coverage, PSB's SED- and F160W SExtractor-inferred B/T agree at $t_{\rm obs}$, suggesting that we can perform reasonable reconstructions for this system.) PAS's progenitor would have had a similar B/T to SSF's but significantly lower sSFR.

In all cases, if anything, B/T decreases with time relative to the (quasi-static; Lang et al. 2014) population locus, if not absolutely. Another expression of inside-out growth, this signals that progenitors of modern galaxies with substantial disks ($B/T \sim 0.4$) may descend from lower-mass galaxies with relatively high B/T. Interestingly, this signal also emerges from at least Morishita et al. (2015)'s cross-sectional, abundance-matched tracks. As discussed regarding CSF, it further suggests that atypically disk-dominated galaxies are a special population. We address this point in Section 5.

4.3.3. Lateral Contamination

A concern regarding the above results is that slices through a galaxy at fixed y cut across many different radii. For a circular object, this effect is obviously most pronounced at $y \approx 0$,

where a section will contain contributions from all radii weighted by the light profile. INNER extractions might therefore reflect conditions at $r \gg 0$, though we have assumed they describe a galaxy's center.

Fortunately, such lateral contamination does not qualitatively affect our findings (see Appendix C and Figure 18 for detailed discussion). First, for all but SSF, a majority of the total INNER light indeed comes from $r \approx 0$ (50% to 70%). In SSF, this region still contributes a plurality ($\gtrsim$40%), readily detectable at the relevant S/N ($\sim$10 pixel^{-1}). Moreover, lateral contamination only makes INNER regions look more like MIDDLE and OUTER ones, and, as just discussed, we see many clear differences in these zones. Hence, this effect serves mainly to turn our inside-out growth assessments into conservative limits. In CSF—the one system where we do not see such differentiation—$\sim$60% of INNER light comes from $r \approx 0$ at S/N $\sim$ 7.5 pixel^{-1}, sufficient to suggest that its inferred SFH spatial uniformity is meaningful (Sections 4.3 and 5.1).

Lateral contamination is unfortunately inescapable in the GLASS data. Sophisticated forward modeling could help disentangle it, but such analyses are beyond the scope of this proof-of-concept. Section 5.2.2 comments further.

5. Discussion

We close by interpreting our results in terms of their astrophysical and methodological/theoretical implications. Astrophysically, we focus on the relationship between B/T and SFH shape, specifically INNER sSFRs rising above global averages at the time of peak SFR, suggesting feedback from bulge building may play a role in quenching as some numerical models posit. We also compare our results to predictions from previous semi-empirical models, which may similarly suggest that particularly disky galaxies—at least as defined relative to equal-mass systems—are a special class. Methodologically, we discuss the limitations of this analysis and what future studies can (and cannot) do to overcome them.

5.1. Astrophysical Implications

5.1.1. Effects at t_{obs}

Figures 4, 6, and 7 touch on basic astrophysical issues. These show that spatially resolved properties at $t_{\rm obs}$ can lead to different physical inferences than integrated measurements. Specifically, (1) galaxies and their components can be classified differently with respect to population loci (e.g., the SFMS); (2) systems with distinct integrated or resolved sSFRs can have similar $\Sigma_{\rm SFR}$; and (3) even at log $M_* \sim 11.2$, AGNs need not rapidly quench star formation at large r (see also Aird et al. 2012; Harrison 2014; Poggianti et al. 2017). Regarding item (1), if SFHs are lognormal, our two star-forming systems go from (somewhat) underperforming pieces to normal wholes at their respective M_*. Note that all of these entities are evolving through—not along—the SFMS at $t_{\rm obs}$, furthering, e.g., Kelson (2014)'s doubts about the profoundness of this locus.

5.1.2. The Epoch of Peak Central Star Formation

Higher-level issues emerge from interrogating Figure 10. In the leftmost panels, Σ_{M_*} at the time of peak INNER SFR (i.e., SFH turnover) is overplotted as vertical orange bands. These span about a factor of three across the sample: log $\Sigma_{M_*} \sim$ 8.5–9. In all but CSF, while INNER regions go on to roughly double in mass,

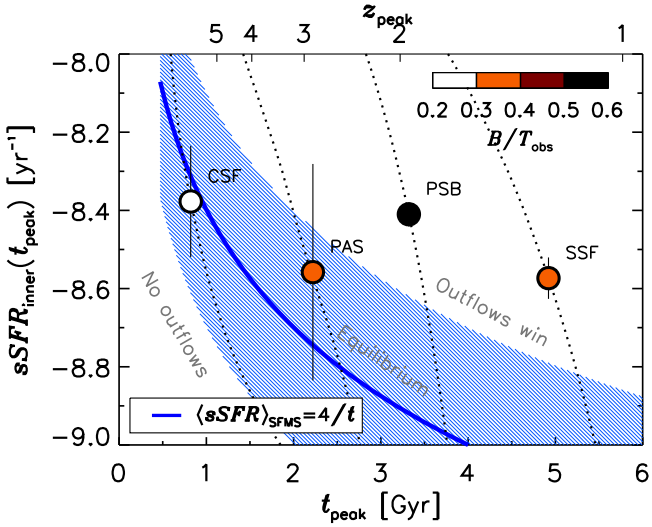

Figure 12. Higher B/T galaxies (point colors) had super-SFMS INNER sSFRs when their SFHs peaked and were always "overactive" according to their median SFH (dotted lines). Conversely, CSF has the lowest B/T and never rose above/has stayed near the SFMS, which was higher at CSF's earlier peak time. If the SFMS reflects inflow/outflow equilibrium (e.g., Davé et al. 2011), this finding suggests a link between bulge building and a feedback-related mechanism turning SFHs over (outflows beat inflows; Zolotov et al. 2015; Tacchella et al. 2016b). Disk galaxies may therefore be objects with flat/quasi-constant SFHs (Figures 9 and 14; Sections 4.3.2, 5.1.2).

this value appears to serve as a sort of boundary beyond which the rest of the galaxy will not pass. This may be a coincidence arising from the small sample size or these galaxies' specific mass profiles, but it may also support recently popular quenching mechanisms where strong outflows at peak INNER SFR induce galaxy-wide quenching. We find evidence for this scenario in a link between high-B/T and falling SFHs, but also for its incompleteness.

Bearing in mind the caveats that come with this sample size, Figure 12 presents our test. It shows each galaxy's INNER sSFR—i.e., SFR per unit of mass/outflow restoring force—at the time of peak INNER SFR plotted against the contemporaneous $\langle$sSFR$\rangle$ of star-forming galaxies (Madau & Dickinson 2014; Kelson 2014) with points coded by $B/T_{\rm obs}$.

Hints indeed emerge that systems with high B/T—especially PSB and SSF—had elevated sSFRs compared to the mean star-forming galaxy at epochs before their SFHs started falling (i.e., quenching). Insofar as the SFMS reflects an equilibrium—where inflows balance outflows (Dutton et al. 2010; Davé et al. 2011)—this suggests that central star formation in these galaxies was strong enough to allow feedback via, e.g., supernova winds to quench their INNER regions, with the rest of the galaxy to follow. This finding would support aspects of the scenarios in Zolotov et al. (2015) and Tacchella et al. (2016b), though, formally, enhanced sSFR($t_{\rm peak}$) reflects a history of super-SFMS activity for a given lognormal SFH, not the last burst in a series of pre-quenching surges. As mentioned (Section 4.3.2), those "compaction" scenarios are also consistent with at least PSB's inferred motion in the r_e–M_*–B/T plane, where it went from being a small, high-sSFR, "overly" bulge-dominated blue nugget to a galaxy with a more normal sSFR for its B/T and size (Barro et al. 2013, 2017a).

CSF also partially supports this scenario by being a good exception to it. The sample's centrally densest galaxy, it also has the highest SFR, lowest B/T ($\sim$0.3), and flattest/largest-τ

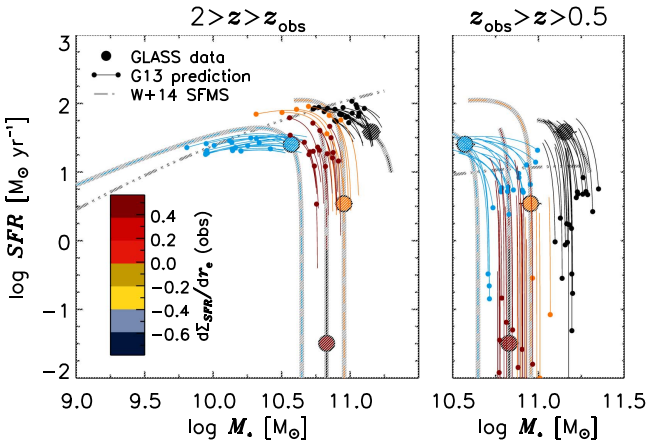

Figure 13. The G13 model SFHs (colored lines/small points) passing through the sample at t_{obs} (large points) projected to show progenitor/descendant envelopes at $z = 2$ (left) and 0.5 (right). Colors show $\Sigma_{SFR}(r; t_{obs})$ data slopes (Figure 7; bluer ↦ more negative). G13 generally captures the data-inferred SFHs, though SSF evolves faster than predicted; both agree that all systems were SFMS galaxies at $z = 2$ (gray dot-dashed lines; Whitaker et al. 2014), except possibly PAS, which may already have shut down. At $z \sim 0.5$, CSF has an ∼50% chance of remaining a massive star-forming galaxy as data reconstructions suggest, while ∼20% of SSF's tracks suggest that it will quench by then. More negative SFR gradients may imply slower evolution—another manifestation of bulge-first growth—but more data are needed to confirm.

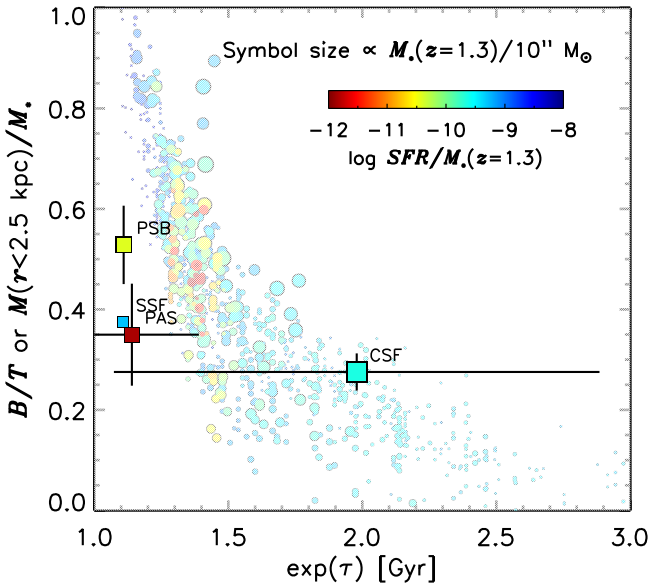

Figure 14. GLASS sample data inferences (squares) vs. G13 B/T–τ predictions (circles; see main text and Abramson et al. 2016's Figure 14 for details). Colors show model $z = 1.27 = \langle z_{GLASS} \rangle$ and observed sSFRs. The data's trend for higher measured B/T to correspond to smaller inferred τ and the corresponding sSFRs is well predicted, though SSF and PSB are quantitatively low. This amplifies Section 5.1.2's discussion of a bulge-growth/SFH shape connection—high (low) B/T implies SFHs that do (do not) turn over—a robust conclusion of this work and an independent consequence of G13. Indeed, if CSF's τ error bar—and perhaps G13's large-τ tail—reflect the fact that they cannot formally be captured by a lognormal, this may suggest that galaxies with near-constant SFHs form a special class.

SFH (Figure 10). While seemingly at odds with the above paradigm, these properties are in fact linked to it through time. Figure 12 shows that CSF peaked early enough that, though it had a high absolute SFR—essentially the same sSFR(t_{peak}) as the other systems—given the prevailing inflow conditions at the time, it need never have left equilibrium. Hence, CSF's center need never have blown itself out (unlike PSB's and SSF's), so it could proceed to grow calmly at all r to t_{obs}, some 4 Gyr (∼4 t_{Hubble}) later, if not today (Figure 13).

This helps explain why CSF's sSFR(r) can be ∼1/3 of SSF's despite its similar $\Sigma_{SFR}(r)$ (Figure 7): it can sustain the "normal" star formation implied by the latter observation because its higher mass was built slowly over Gyr from a gentle SFH, not rapidly via a violent one leading to equilibrium-breaking outflows. This scenario—that both the time and timescale of star formation are critical—is precisely the mathematical premise of Gladders et al. (2013, hereafter G13), and the above is qualitatively consistent with previous arguments linking bulge growth to its SFHs' shapes (Abramson et al. 2016; Section 5.1.3). If correct, these findings highlight the centrality of path dependence in galaxy evolution and the need for future similar analyses. They also suggest that additional density-independent but time-dependent processes must be invoked to shut CSF down whenever that happens (e.g., Larson et al. 1980; Croton et al. 2006; Peng et al. 2015; Voit et al. 2015; Oemler et al. 2017).

How PAS fits into this story is unclear given the uncertainties and the SFMS's width. While it seems more likely to have been in the "overly productive" regime of the later-peaking SSF and PSB, a robust conclusion—as well as more representative empirical inferences—requires additional data.

One last point is worth noting: irrespective of its sSFR at any t, to the extent that lognormal SFHs reflect reality, the mode galaxy will grow by ∼2.5× after peak SFR. While it may take Gyr for it to attain that asymptote—over which it will have a substantial SFR—this corresponds to just 0.4 dex on a log M_* abscissa (Figure 10). As such, for any SFH with a declining tail, the quenching process will almost always appear rapid. Corollary to the SFMS case, this phenomenon erodes the informativeness of the bimodal quenched/star-forming dichotomy: even robustly star-forming galaxies—those at peak SFR—might reasonably be "quenched" from the perspective of future M_* growth. While perhaps useful for modeling, e.g., the evolution of mass functions, it is difficult to see how such a division illuminates the processes controlling star formation. Regardless, in any framework, the above suggests that studying systems with rising SFHs will be more edifying, which are by definition low-mass. SSF's progenitors—log(r_e, M_*, SFR) ∼ (0.4, 9, 1) with high B/T—seem good $z \sim 2$ follow-up candidates by which to infer the development of some of today's MW-mass galaxies (Figures 4, 7, 11, and 13).

5.1.3. Relationship to Previous Model Predictions

In the size–mass context, Figure 11 suggests the obvious comparison between these galaxies' longitudinally inferred trajectories and, e.g., Morishita et al. (2015, hereafter M15)'s abundance-matched cross-sectional inferences for the mean system of similar mass. Clearly, these methods yield different size projections: SSF and CSF have identical masses to M15's means at t_{obs}, but they are both observed to be and inferred to remain smaller than what that study would predict. This is despite the fact that M15 captures CSF's size at $t_{obs} - 1$ Gyr.

Certainly, part of the discrepancy could simply be that our sample is not average. Further, M15's cross-sectional method captures ex situ growth from mergers—which we cannot—and our rather coarse radial resolution limits size-growth sensitivity. However, if substantiated by larger analyses, such tension would point to a meaningful divergence between the evolution

of the mean size of galaxies and the size evolution of the typical (i.e., mode) galaxy. This said, B/T inferences seem more robust to the above issues, agreeing better qualitatively—and quantitatively, at least at $t_{\rm obs}$—than sizes. We do not know why this is true, but it is intriguing.

If borne out in the future, Figure 11 (left)'s r–M_* reconstructions would also disfavor a suite of analytic prescriptions (Bezanson et al. 2009; van Dokkum et al. 2015; Abramson & Morishita 2018; Lilly & Carollo 2016) wherein galaxies grow at roughly fixed σ_v, ρ_{M_*}, $\Sigma_{M_*}(r < r_e)$, or $\propto M_*^{1/3}(1+z)^{-1}$, corresponding, respectively, to tracks with slope 1, 1/3, 1/2, and ∼0.7 in that plane. These are far steeper than our inferences. Conversely, our tracks are not too dissimilar from the Illustris simulation's flatter $r(M_*)$ trajectories (Genel et al. 2018; see their Figure 4). In all cases, future longitudinal comparisons should have great potential here (Section 5.2).

Beyond such semi-empirical comparisons, we can explore how our inferences compare to the G13 global lognormal SFH model itself. This was the source of our SFH parameterization, and Abramson et al. (2016) specified ways to falsify it using these kinds of data (see their Appendix A).

The first test states that G13 would be ruled out if:

> Large, abrupt discontinuities are required to explain a significant fraction of SFHs for systems dominating the universe's mass and star formation budget over a significant fraction of cosmic time (smooth, continuous parameterizations cannot describe most SFHs).

Of this sample's four galaxies, one—the post-starburst PSB—has SEDs that significantly disfavor lognormal SFHs in the UV at all r probed due to what was likely an abrupt SFR shutdown <1 Gyr before $t_{\rm obs}$ (Figures 1 and 2). One could thus posit that 25% of galaxies—perhaps 50% of passive ones—at $z \gtrsim 1$ and $\log M_* > 10.5$ may therefore require such events. If more data support this conclusion, it would seriously challenge G13's limited view of the role of SFH discontinuities.[16]

On the other hand, PSB's MOSFIRE-derived Balmer lines are, if anything, weaker than the best-fit lognormal implies, suggesting that any discontinuity occurred farther from peak SFR than we conclude from the *HST* data alone (Figure 8; Table 3). This would make the natural lognormal falloff responsible for a larger portion of PSB's decline. Also, by assuming solar metallicity, we may have underestimated PSB's true metal content and thus UV line blanketing (Gallazzi et al. 2014). Third, we may simply have caught an unrepresentative system in our sample.

Two additional tests suggest that, if it is wrong about the relevance of discontinuities, G13 still captures key aspects of these data's story. Figure 13 compares the sample integrated SFHs to G13 model tracks passing within 2σ of the galaxies' observed (M_*, SFR)($t_{\rm obs}$) coordinate/limit. The left panel projects the models back to $z = 2$, and the right one projects forward to $z = 0.5$. Color-coding reflects the slope of the data's observed SFR surface density profiles. In this independent cross-check, G13's high-z predictions match the data inferences to within about a factor of two in both axes in all but SSF, which grows much faster than the model tracks. Given that G13 was based on no SED fits and contained no data-derived SFH information whatsoever, this level of agreement is encouraging.

Looking ahead to $z = 0.5$, the model also does reasonably well, if perhaps in a more probabilistic sense. Around 20% of model SFHs passing near SSF at $t_{\rm obs}$ suggest it will become a passive, $\log M_* \sim 10.7$ low-z galaxy, $\sim 1.3\sigma$ agreement with its (median) data-inferred trajectory. Similarly, about half of the CSF-matching trajectories suggest it will remain a massive, star-forming system. Clearly, all inferences agree that PSB and PAS will become ∼M31- and MW-mass passive systems. Note that these statements are converse to those in Section 4.1.2. Figure 4 shows where $z = 0$–selected MW-mass progenitors lie at a mean sample redshift; Figure 13 shows where the descendants of $z > 1$–selected galaxies lie closer to today.

In terms of informing future G13-like modeling, the spatially resolved data suggest a $d\mathrm{sSFR}/dt$–$d\Sigma_{\rm SFR}/dr(t_{\rm obs})$ anticorrelation, such that galaxies with the least-negative SFR gradients are evolving the fastest (yet another restatement of inside-out growth). However, SSF's data buck this trend, so robust statements await larger samples.

Figure 14 presents a final test. Here we plot the data against the B/T–τ prediction from Abramson et al. (2016; see their Figure 13). The latter was calibrated at $z = 0$ by rank ordering G13 τ and Gadotti (2009) B/T measurements at fixed M_*, assuming the smallest τ corresponds to the largest B/T. Point colors reflect the $z = 1.27 = \langle z_{\rm GLASS} \rangle$ model and observed sSFRs. Since no information on the y-axis was used in its construction, the properties of this locus represent blind predictions of the G13 model. As such, this comparison is a true experiment.

Two points are salient. First, the general B/T–τ trends in the data reflect those in the G13 model: smaller inferred τ is associated with systems of higher measured B/T. Second, the sample's measured sSFRs (point colors) are consistent with those of the G13 tracks at the appropriate B/T, though they are likely more massive than the typical model at that y location, and SSF and PSB have quantitatively lower τ than predicted. The lowest-B/T sample galaxy, CSF, is especially well-matched in this regard. Considering the model locus was calibrated at $z = 0$—some 8 Gyr after the epoch probed here—we consider even this level of agreement striking. (Given their declining SFHs, the GLASS sample's B/T should evolve little between $t_{\rm obs}$ and today (Figure 10).)

If supported by larger future data sets, the implications of especially CSF's location in Figure 14 amplify Section 5.1.2's discussion of the connection between B/T and SFH shape as captured by τ, the star formation timescale. Apparently, G13 prefers galaxies with $\exp(\tau) \gtrsim 1.5$ Gyr—i.e., the flattest SFHs—to be the most disk-dominated, even if they are relatively massive.[17] This link between high (low) B/T and SFHs that do (do not) turn over is perhaps the central physical inference of this work and an independent feature of G13.

Now, G13 did not attempt to show that the lognormal was the best SFH parameterization, nor do we know how many of their findings could also be derived using, e.g., triangles or any other time-asymmetric SFH (Abramson et al. 2016).

[16] Strong Balmer absorption is common in red galaxies at these and higher z (e.g., van de Sande et al. 2013; Whitaker et al. 2013; Newman et al. 2014; Belli et al. 2017), but it is unclear if these signatures cannot be produced by smoothly rising and falling histories at such early epochs.

[17] Truly constant SFHs cannot formally be captured in the lognormal framework. It is thus interesting to consider whether the large-τ tail in the G13 locus in Figure 14—or even CSF's τ error bar—fundamentally highlights a physical regime in which this paradigm breaks down (or something more abstract). If so, SFHs approaching this limit may form a special class. We encourage further investigation in this vein.

Nevertheless, we think it is fair to say that the above SED-based tests independently support G13's non-SED-based model (at least in spirit), though we cannot claim that they reveal a deeper underlying physicality to the lognormal SFH.

5.2. Implications for Methods and Theory

5.2.1. Future Applications

While other studies have used similar spectrophotometric data to reconstruct aspects of galaxies' longitudinal evolution at $z > 1$ (Whitaker et al. 2013; Newman et al. 2014; Domínguez Sánchez et al. 2016; Nelson et al. 2016a; Lee-Brown et al. 2017; Toft et al. 2017), S/N and spatial resolution limitations have forced these to rely on stacks, treat galaxies as monolithic objects, or quote SFH summary statistics (e.g., age). By exploiting gravitational lensing and GLASS's depth, this is, as far as we are aware, the first $z > 1$ study to perform a full, spatiotemporally resolved, spectral continuum SFH reconstruction for individual galaxies to $r \sim 2\,r_e$.

To progress, more such (or better) information will be essential: Figures 7, 9, 10, and 11 are (hopefully) crude representations of the kind of empirical inferences that can ultimately constrain the galaxy evolution narrative. Indeed, next-generation facilities will likely make this type of analysis routine. With its redder, higher spectral and spatial resolution slitless grisms, slit spectrographs, IFU, and imagers, *JWST* could apply more sophisticated versions —incorporating new insights into spatially variable emission-line interpretations (Sanders et al. 2017)—to practically any suitably bright $z \gtrsim 0.7$ system. Further, it will extend samples vastly in redshift and provide critical spatially resolved M_* constraints from rest-IR photometry that do not yet exist (and whose absence is a key weakness of this study).

WFIRST will more directly translate our methodology but over huge areas of the sky, enabling tests of the critical galaxy–environment connection (perhaps the key issue; Dressler 1980; Kelson et al. 2016). Combined with 30 m class telescope observations of specific targets—which will replicate some of *JWST*'s capabilities but at higher spatial resolution given planned adaptive optics—this may prove revolutionary. Lastly, as envisioned, spectrographs on all of the above platforms will measure spatially resolved stellar absorption lines, providing more robust SFH and metallicity constraints (e.g., Figure 8; Worthey et al. 1992; Trager et al. 1998), another datum we could not incorporate here. To our knowledge, Newman et al. (2015) and Toft et al. (2017) presented the only such observations at $z > 1$ for two log $M_* \sim 11.1$–11.5 lensed systems, with LEGA-C (van der Wel et al. 2016) just now providing the first statistical database at $z \sim 0.7$. Next-generation facilities may make such data the norm.

Other meaningful immediate advances include moving to true radial reconstructions using IFUs; building a chordal-to-radial transformation calibration library using, e.g., GALFIT (Peng et al. 2002) or performing full forward modeling to ameliorate the lateral contamination issues we could not avoid (Section 4.3.3); and exploring the effects of moving from parameterized to free-form SFHs. The latter were adopted by the *Carnegie Spitzer IMACS Survey* (Kelson et al. 2014; Dressler et al. 2016; Dressler et al. 2018), and this and similar approaches based on halo merger-tree motivated SFHs (Pacifici et al. 2013, 2016) and fine landscapes of basis functions (Iyer & Gawiser 2017) are proving powerful. Specifically, these methods have the advantage of avoiding the assumption that SFHs must rise and fall/each phase's relative mass contribution. They also allow each SFH component to have its own A_V and metallicity, enabling self-consistent chemical enrichment and mass growth modeling (Muñoz & Peeples 2015). Both effects have potentially important ramifications we could not assess, and, though SFH discontinuities may complicate temporal, e.g., size reconstructions, further study will be fruitful.

5.2.2. Irreducible Uncertainties

Despite the above advances, a core issue will accompany all future work. Assuming the above techniques yield consensus SFHs when applied to data of suitable quality, and irrespective of whether those data are resolved radially, in sections, or treated as independent spaxels, the results will never correspond to the evolution of the matter in that aperture. Rather, they will reflect the evolution of the aperture based on its contents at $t_{\rm obs}$. Because we only ever get one look at a galaxy, regardless of the fineness of the empirical mesh, inferences derived therefrom must follow from each cell's state at one and only one instant. Yet the galaxies themselves are collections of moving elements, so the stars/gas we aim to characterize may never occupy that cell at any other epoch. This fact—which also forces assumptions about the role of mergers, which contribute to mass growth without leaving unique spectral signatures—has been an ever-present if inevitable issue here, whose effects only forward modeling can constrain.

Of course, it may be that, once $t_{\rm Dyn} \ll t_{\rm Hubble}$ (which occurs quite early), material is moving so swiftly compared to the timescales of interest that the above effects "smooth out" (at least in some mathematically tractable sense), permitting the recovery of meaningful, azimuthally averaged histories. Or, due to, e.g., secular evolution/radial migration, they may not (e.g., Garrison-Kimmel et al. 2017). Either way, observers and simulators should work together to understand and constrain the effects of this fundamental empirical limitation, thus clarifying when to conclude the project of understanding how galaxies' biographies led them to their observed states.

6. Summary

Based on deep, 17-band CLASH/HFF+G102/141 GLASS *HST* spectrophotometry, we reconstruct the integrated and spatially resolved SFHs of four $z \sim 1.3$ cluster-lensed galaxies (Table 1) using full-spectrum, rest-UV/-optical fitting at $|r| \lesssim 2\,r_e$. The sample spans log $M_* \simeq 10.5$–11.2 and contains one anciently passive, one recently quenched, one continuously star-forming, and one SSF galaxy (Table 2; Section 4.1), enabling these case studies to probe spatiotemporal phenomena relevant to meaningful parts of parameter space (MW- to super-M31-mass progenitors; Figure 4). Our work has three main implications.

Methodologically, the best current data enable observers to resolve galaxies in both space and time, offering new ways to empirically connect their observed properties—here r_e, B/T, $\Sigma_{M_*}(r)$, and $\Sigma_{\rm SFR}(r)$ (Section 4.2, Figure 7); perhaps one day $A_V(r)$ and $Z(r)$—to aspects of their individual histories, moving data-driven inferences much closer to the domain of theoretical models. We demonstrate this using just three radial bins and the assumption of lognormal SFHs (Sections 2, 3), but future IFU studies or different SED fitting techniques could relax these constraints, enabling robust assessments of the dependence of astrophysical conclusions on such factors.

Astrophysically, we find hints of a connection between B/T and SFH shape/spatial uniformity (Sections 4.3, 5.1). The three sample

galaxies with the highest B/T are also those showing signs of inside-out growth—where the INNER regions move from leading to lagging those at larger r in SFR(t)—and indeed those with obviously rising and falling SFHs (Figures 5, 9 and 10). Further, two of these are inferred to have had sSFRs well above the SFMS at the time of peak INNER SFR (with the other marginally elevated). This is to be contrasted with the diskiest system ($B/T \sim 0.3$), which had a spatially uniform, slowly declining SFH that never exceeded the mean sSFR of all star-forming galaxies (Figure 12). Both signals are consistent with recent theoretical suggestions positing a link between bulge growth and SFR declines (Zolotov et al. 2015; Tacchella et al. 2016b).

Further, individual size and B/T evolutionary trajectories may diverge from cross-sectional inferences based on abundance matching (cf. Morishita et al. 2015, and Figure 11 above), emphasizing the temporal diversity underlying single-epoch galaxy parameter projections. Half-mass radii are inferred to evolve negligibly across at least the 2 Gyr bracketing $t_{\rm obs}$, even as galaxies gain factors of $\sim$6 in M_* over the same period. Similarly, B/T evolution may be flat or decreasing in an absolute sense—suggestive of inside-out growth—but is more robustly negative relative to the mean at a given M_*; i.e., sample galaxies tend to start above the B/T–M_* locus at low mass but end up at the appropriate value at their terminal masses, in closer agreement with M15's cross-sectional inferences.

While sample size forces these statements to remain tentative, *JWST*, *WFIRST*, and the 30 m class telescopes will routinely produce data that can support this and more sophisticated analyses and therefore contextualize or refute them.

Finally, information-theoretically, empirical spatiotemporal inferences will ultimately be limited in that they must forever be based on the matter in an aperture at one and only one epoch. As such, even given arbitrarily well-resolved, high-S/N IFU data and no systematic uncertainties (e.g., as to the IMF or chemical evolution), the fundamentally Eulerian nature of data-driven reconstructions will always place them in a slightly different domain (aperture evolution) than the Lagrangian theories they should be used to test (galaxy evolution). Understanding the relationship between these two entities will require the joint efforts of theorists and observers working toward a common interpretive framework. We are hopeful such partnerships will soon emerge, ushering in a qualitatively new relationship between data and theory.

LEA thanks D. Kelson, J. Mirocha, and S. Birrer for their tolerance during many enlightening conversations. The same goes for L. Young, who illuminated key longitudinal/cross-sectional distinctions underpinning this work, and M. Gladders, whose ideas were central to it. We also thank the anonymous referee for helpful and incisive comments. BV acknowledges support from an Australian Research Council Discovery Early Career Researcher Award (PD0028506). GLASS (*HST* GO-13459) is supported by NASA through a grant from STScI operated by AURA under contract NAS 5-26555. This work uses gravitational-lensing models by PIs Bradač Natarajan & Kneib (CATS), Merten & Zitrin, Sharon, Williams, Keeton, Bernstein & Diego, and the GLAFIC group. Lens modeling was partially funded by STScI's *HST* Frontier Fields program; models were obtained from the Mikulski Archive for Space Telescopes (MAST).

Facilities: HST ACS/WFC3, Keck MOSFIRE.

Software: IDL Coyote (D. Fanning; http://www.idlcoyote.com) and MPFIT (Markwardt 2009) packages; SAO DS9.

Appendix A
Data Structures

Spectra.—The GLASS pipeline outputs a FITS cube for each source in each grism at each orientation. The files contain the following objects/data types.

1. DSCI—Direct image of each source taken from a CLASH or HFF WFC3IR image stack to which the GLASS full-field grism frames are aligned/referenced (60 × 60 pixel image; "DIRECT_IMAGE" in text).
2. DWHT—DSCI's rms error map (60 × 60 pixel image).
3. SCI—Cutout of the full-field GLASS grism image containing a target's 2D spectrum (360 × 60 pixel image).
4. MODEL—Model of the target's spectrum in SCI; based on the CLASH/HFF alignment image SExtractor segmentation map (360 × 60 pixel image).
5. CONTAM—Model of all nontarget spectra in SCI; based on the CLASH/HFF alignment image SExtractor segmentation map (360 × 60 pixel image).
6. WHT—SCI's rms error map (360 × 60 pixel image).
7. YTRACE—Centerline of the target's 2D spectrum (spectra are not rectified; 360 element array).
8. SENS—1D grism response curve along YTRACE ($e^-/{\rm s} \rightarrow 10^{-17}$ erg s^{-1} cm^{-2} Å^{-1}; 360 element array).
9. WAVE—$\lambda(x)$ [Å] along YTRACE (360 element array).

All 2D data derive from interlaced—not drizzled—WFC3IR reductions, maintaining pixel-to-pixel independence. The 1D spectra derive from the SCI minus CONTAM image, masking SCI = 0 pixel, and those with CONTAM $\geqslant 2 \times$ WHT && CONTAM/MODEL $\geqslant 0.01$ (i.e., pixels with significant contamination bright enough compared to the target to cause meaningful continuum biases over $\sim$100 pixel extents). Quality control (Section 2.2) ensures masking is minimal for the sources in this study, but it is visible, e.g., in the OUTER zone of CSF (Figure 2).

Spectral extraction boxes are centered on and reflected over YTRACE(x) with widths set by r_e as measured from DSCI (Section 2.3). Spectral uncertainties at each λ are the quadrature sum of WHT(x) over all unmasked y in the extraction zone. Figure 15 shows the distributions of per-pixel S/N for the resulting 1D spectra.

For the optimal extractions, each column of a SCI-sized image is filled with an object's normalized 1D spatial profile centered on YTRACE(x). This weights the SCI − CONTAM flux sum over all $N \leqslant 60$ unmasked y pixels at each x (Horne 1986).

This process is repeated independently in G102 and G141, producing a pair of spectra and LSFs for each zone of each object (see Fgiure 16). These are sent to *pyspecfit* simultaneously, along with multiband, aperture-matched CLASH +HFF photometry.

Photometry.—In addition to the spectra, $N = 17$ band image stacks are also cut for each source from PSF-matched (F160W resolution) CLASH/HFF imaging (Morishita et al. 2017). These and their weight maps are rebinned from their native 0.″06 to GLASS's 0.″065 pixel scale and rotated to the GLASS DSCI image orientation by finding the angle $\theta/{\rm deg} \in [0,359]$ that minimizes

$$\chi^2_\theta = \sum_{\rm pix} \frac{(I^{\rm NIR}_\theta - {\rm DSCI})^2}{{\rm DWHT}^2}, \quad (2)$$

where $I^{\rm NIR}_\theta$ is a stack of the F105–160W CLASH/HFF stamps (rotated by θ). The best-fit θ is applied to each CLASH/HFF

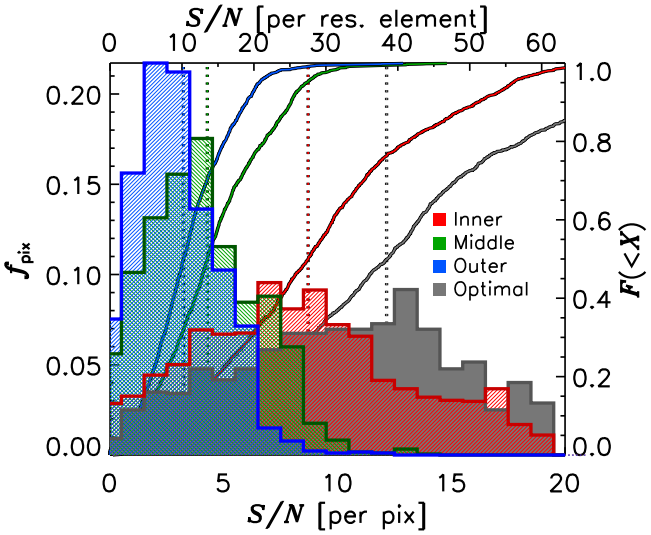

Figure 15. The S/N distributions for the 16 sample spectra (four per galaxy). INNER (red) covers $|r/r_e| \lesssim 0.4$; MIDDLE (green) and OUTER (blue) reach $|r/r_e| \in (0.4, 1.0]$ and (1,2], respectively. Optimal extractions are plotted in gray. Dotted vertical lines show the median S/N.

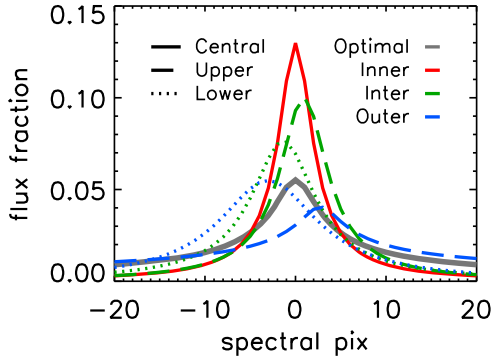

Figure 16. LSFs for CSF's unfolded radial and optimal extractions showing offsets and chord profile variations (Section 2.3). These preclude a priori impositions of symmetry in objects with PA $\sim 45°$.

image individually. This angle will generally not correspond to the GLASS orientation—the *HST* roll angle when the spectra were taken—as DSCI is from an independent alignment image. Pixel interpolation is cubic.

Once properly orientated, each band of CLASH/HFF imaging is photometered in the same zones as the spectral extractions. We assume YTRACE follows the NIR image centroid, which we find using SExtractor on the rotated F105–160W stamp stack, $I^{\rm NIR}$. As with θ, we fix this centroid to $r = 0$ in all bands (in the blue, prominent star-forming regions can and do shift independent SExtractor X_ and Y_IMAGE estimates). The r_e-based extraction zone offsets derived from the DSCI light profile (Section 2.3) are then applied based on this centroid, and all flux in the CLASH/HFF stamp is summed within each zone ($60 \times y_{\rm zone}$ pixel^2 aperture). Comparisons to synthetic photometry derived directly from the GLASS spectra suggest that this process is absolutely accurate to within $\pm\sim$30% (1.5σ). Regardless, the spectra are scaled to the photometry—which is corrected for galactic extinction—during SED fitting (Section 3). Figures 1 and 2 demonstrate that relative spectrophotometric accuracy is excellent.

Appendix B
Further Details on Spectral Synthesis Modeling

B.1. Fitting Scheme

The fitting scheme is as follows.

1. Assume a delayed exponential SFH,

$$\mathrm{SFR}(t) \propto \frac{t - t_{\rm start}}{\tau_{\rm exp}^2} \exp\left[-\frac{t - t_{\rm start}}{\tau_{\rm exp}}\right], \quad (3)$$

   where t is cosmic time, $\tau_{\rm exp}$ is an e-folding timescale, and $t_{\rm start}$ is the beginning of the SFH. See Appendix D for $\tau_{\rm exp}$ and age ($= t_{\rm obs} - t_{\rm start}$) trends.
2. Find the galaxy's global redshift and integrated properties using the optimal extraction.
3. Find the redshift and properties of the INNER extraction using the redshift from step 2 as a strong prior.
4. Lock the MIDDLE and OUTER extractions to INNER's redshift, shifting the traces by the offsets identified during LSF measurement if these are larger than the formal z uncertainty (Section 2.3).
5. Find the properties of the MIDDLE and OUTER extractions given the central redshift solution.
6. Repeat steps 2–5, assuming a lognormal SFH fixed to the correct redshift.

B.2. Fitting Parameters

Details differ slightly depending on the SFH, but the full parameter and prior set is as follows.

1. Redshift (z) in the case of the delayed exponential model and optimal/INNER extractions. Broad Gaussian prior based on GLASS database redshifts.
2. Stellar mass (M_*) and SFR in all cases. No prior; the other parameters fix sSFR and M^*/L, such that SFR and M_* reflect a constant scaling to the overall flux levels.
3. Equivalent widths and fluxes for Hα, Hβ, [O III] $\lambda\lambda$4959, 5007, [S II] $\lambda\lambda$6718, 6733 in all cases. Uniform priors from [0, 500] Å for Hα and [O III]; [0, 50] Å for [S II]. Balmer ratios fixed to unextinguished values in the delayed exponential SFH; free for lognormals.
4. Dust extinction to the stellar continuum, A_V. Uniform [0, 3] mag prior; Calzetti et al. (2000) reddening law.
5. SFH parameters—(age, $\tau_{\rm exp}$) or (T_0, τ) for delayed exponential and lognormal parameterizations, respectively. Priors are: age—log-uniform in [10^7, 10^{10}] yr; $\tau_{\rm exp}$—log-uniform in [10^7, 10^{10}] yr; T_0—log-uniform in [10^9, 10^{10}] yr; τ—uniform in [0.1, 3] (scale factor).

All SED information is considered jointly; spectra are fit at the pixel level along with the broadband photometry. Both data sets are treated independently with their own χ^2 statistics, whose unweighted sum is minimized. As such, each measurement appropriately contributes to the fit in overlapping regions (F814W and redward). Given that spectral elements vastly outnumber photometric points ($N_{\rm phot} = 6$) in the overlap window, the former dominates the likelihood calculation.

Emission lines are fit jointly with the stellar continuum/corresponding absorption. All lines are given the shape of the relevant zone's LSF—i.e., a Moffat profile—with amplitudes adjusted to match the data. The lines themselves are therefore symmetric. However, by including the elements of various

complexes ([O III]+Hβ, [N II]+Hα+[S II]), the fits capture asymmetries arising from line blending at the *HST* grism's low resolution. Beyond CSF AGN identification (Figure 6) and gross EW(Hα+[N II]) trends (Figure 20), we defer a discussion of these to a later paper.

All fitting uses a χ^2 likelihood function (see Appendix B of Newman et al. 2014), but we quote the medians of the resulting posterior distributions as parameter estimates, which are more robust than those from the best-fit model.

Appendix C
SFH Reconstruction Self-consistency

A concern may be that inferences derived from summing the INNER, MIDDLE, and OUTER results diverge from those based on the integrated optimal extractions. At $\lesssim 1.2\sigma$, this is not the case at $t_{\rm obs}$ and, fortunately, over much of cosmic time.

Figure 17 presents this cross-check, showing SFR(t) and $M_*(t)$ inferred from the integrated versus summed resolved results. These are consistent, albeit within large uncertainties on the sums for the passive PAS and PSB systems. The fact that all four galaxies are past their peak SFRs (Figure 9) is brought to the fore here, with no system likely to gain "substantial" mass in the future. This highlights a meaningful distinction between star-forming and rapidly growing galaxies—those with rising SFHs (Sections 4.3.2, 5)—but the agreement between integrated and summed inferences when SSF and PSB were rapidly growing is nevertheless reassuring.

A final concern is lateral light contamination, which might cause INNER extractions to be unrepresentative of galaxy centers, as we implicitly assumed (Section 4.3.3). To quantify this effect, we sliced the INNER extractions from the $I_\theta^{\rm NIR}$ image stacks into the same INNER, MIDDLE, and OUTER bins as we did the vertical profiles in the main analysis (rotated by 90°). We then counted the fractional light contribution in each zone (INNER-INNER, 2 × MIDDLE-INNER, 2 × OUTER-INNER), as shown in Figure 18. (Integrating the INNER LSFs yields similar results.) In all but SSF, 50%–70% of the total INNER ($y \approx 0$) light indeed comes from the INNER-INNER ($r \approx 0$) region. The situation for SSF is worse, with its INNER-INNER box contributing ∼40% of the total INNER light.

While suboptimal, three factors moderate the impact of this finding/lateral contamination in general. (1) In all cases including SSF, INNER extraction S/N is sufficient to provide $>1.5\sigma$ purchase on INNER-INNER properties (e.g., S/N $\geqslant$ 10 pixel^{-1} for SSF's worst-case 35% INNER-INNER contribution). (2) We only compare INNER results to MIDDLE or OUTER ones, not their sum, and INNER-INNER regions are always 50% to >3× brighter than the next brightest (MIDDLE-INNER) slice. (3) Regardless of the above, the most critical impact of contamination would be on inferences of null radial (SFH) gradients, since such apparent spatial uniformity might be due purely to lateral contamination. Only CSF falls in this category, but its INNER-INNER extraction is ∼55% of its total INNER flux and twice as bright as any other zone. Hence, CSF's results should mainly reflect real spatial homogeneity, not lateral contamination, keeping our inferences secure. In the other cases, the effect is to turn the detected inside-out growth signals into ($\gtrsim 1.2\sigma$) lower limits, skewing those findings (somewhat) conservative.

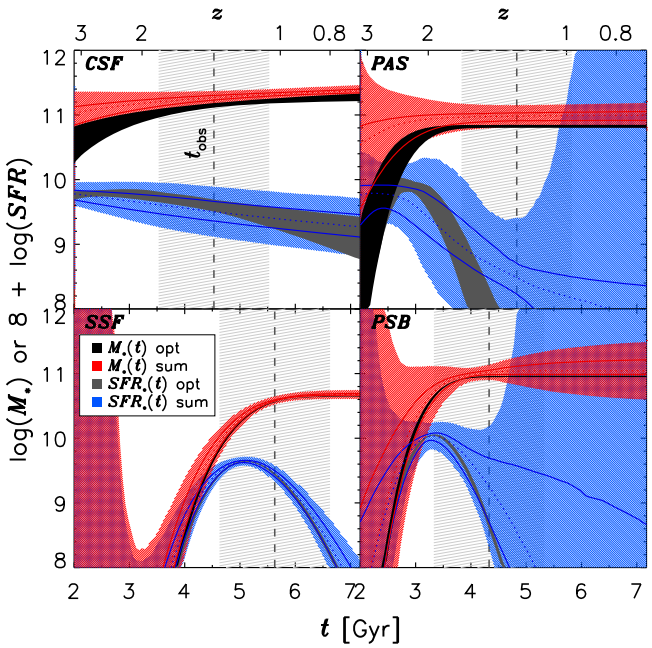

Figure 17. The SFHs and mass growth curves from the optimal integrated extractions (black/gray, respectively) vs. those summing INNER, 2× MIDDLE, and 2× OUTER results (blue/red, respectively). Vertical dashes show $t_{\rm obs}$ with the ±1 Gyr projection window shaded (Section 4.3.2). The 1σ summed uncertainties are calculated as a fraction of the median (shading) and as the log of the high/low linear SFR(t) or $M_*(t)$ estimates (solid lines). The former leads to mostly unconstrained (future) summed uncertainties for PAS and PSB due to their low SFR($t_{\rm obs}$). Even so, the largely independent sums of the parts and inferences from the whole broadly agree.

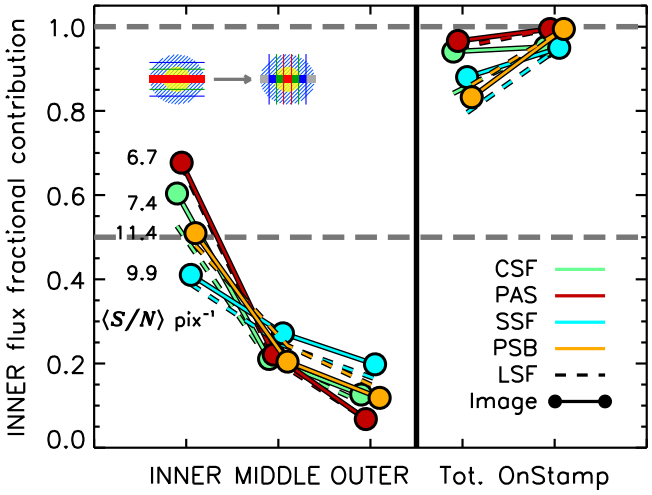

Figure 18. Contributions to the INNER regions' spectra from all regions (assuming $y \mapsto x$ symmetry; see inset cartoon). This is a metric of how closely our chord-based extraction ($y \sim 0$) mimics a true radial one ($r \sim 0$). INNER light dominates this slice in all objects but SSF, where it contributes 35%–40%. However, per-pixel S/N is sufficient to grant $\geqslant 1.5\sigma$ purchase on the effect of this plurality contribution, which manifests in SSF's clear signs of differential central/outskirts growth (e.g., Figure 10). Lateral contamination makes such inferences a lower limit. Conversely, the spatial uniformity of CSF's SFHs should not be a result of INNER contamination given its INNER-INNER region's majority contribution. The three zones capture 80%–95% of the total flux, with >95% contained in the GLASS postage stamps.

Appendix D
Delayed Exponential Results Summary

Figure 19 shows some relevant results based on the delayed exponential SFHs not used in the main analysis. The top panel

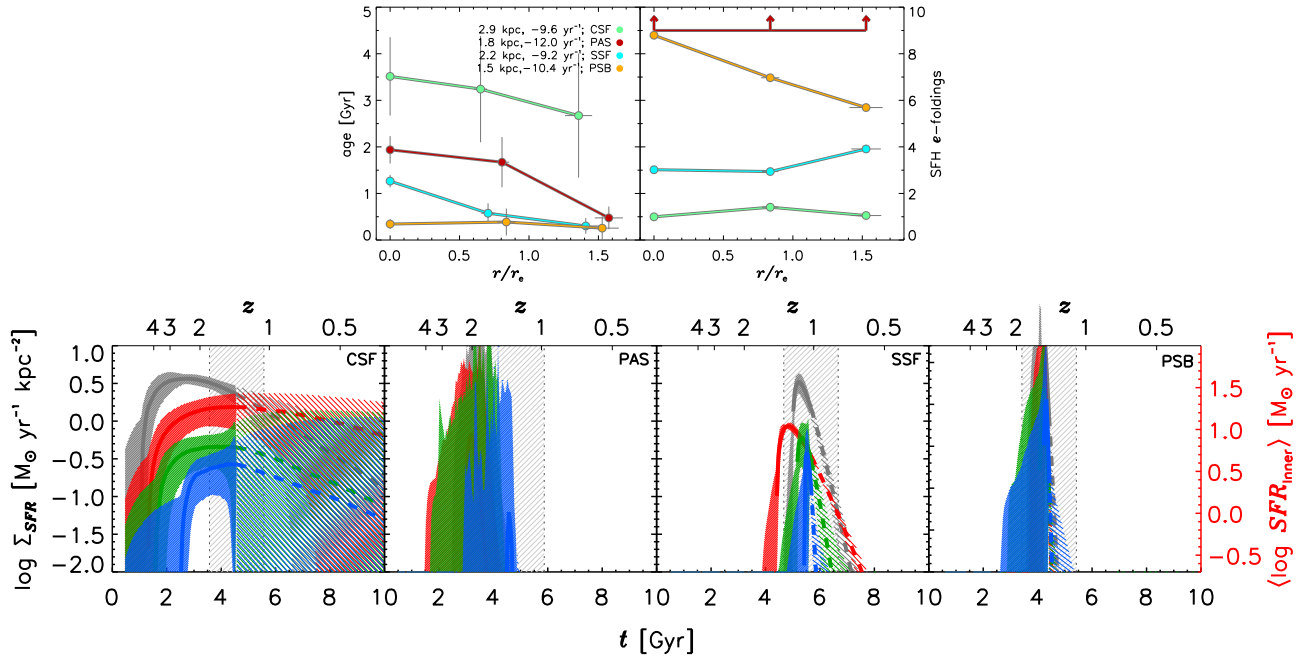

Figure 19. Summary plots based on the delayed exponential SFH fits (Section 3). The top panels show radial parameter trends—age $\equiv t_{\rm obs} - t_{\rm start}$, e-foldings $=$ age$/\tau_{\rm exp}$—that reveal similar signatures of inside-out growth to the main lognormal analysis (INNER regions older/having undergone more e-foldings). The bottom panels reproduce Figure 9, showing the SFHs in full. These qualitatively reflect the lognormal results for CSF's and SSF's INNER region, but PSB and PAS become essentially a convolution of δ-functions, implying unrealistic growth rates in PSB's case and forbidding time-domain reconstructions. Note that inferences such as the INNER/OUTER SFH crossing epoch (inside-out transition) in SSF agree using either method (cf. Figure 10).

shows spatially resolved age inferences (left; age $\equiv t_{\rm obs} - t_{\rm start}$; Equation (3)) and e-foldings (right; age$/\tau_{\rm exp}$). The bottom panel shows the resolved SFHs themselves (replicating Figure 9).

A similar picture emerges from these panels as with the lognormal SFHs, though it is expressed slightly differently/less conveniently given our intent. First, from the top left panel, inside-out age gradients characterize PAS and SSF (INNER regions are oldest). Though unlike in the main analysis, PSB does not appear to have such a gradient, the top right panel pushes back on this, showing an inside-out e-folding, i.e., maturity gradient (INNER regions most evolved).

Figure 19 (bottom) elaborates on this swap: PSB has δ-function-like (zero-age) best-fit exponential SFHs. This follows from discussions in Sections 4.1, 4.2 regarding how this form expresses what is likely an abruptly truncated (post-starburst) SFH. The other systems have e-folding trends that mimic the lognormal inferences, with the star-forming systems having fewer (i.e., wider SFHs) and PAS having the most.

Indeed, the star-forming delayed exponential SFHs grossly correspond to the lognormals (Figure 9), especially for CSF, where the same quasi-flat, rank-ordered SFHs emerge at all r. SSF has similar INNER properties, but to capture this system's sSFR gradient (Figure 7), the MIDDLE and OUTER SFHs become dramatically compressed, illustrating this form's expression of inside-out growth. (Note, however, that SSF's INNER SFH still moves from a leading to a lagging position roughly at $t_{\rm obs}$, as in Figure 10.) The abruptness of these histories—and those for the passive systems—contributes to our disfavoring them for the time-domain reconstructions that are at the core of the main analysis.

Appendix E
EW(Hα+[N II]) Trends, $\Sigma_{M_*}(r)$ in Physical Radii, and the $z \gtrsim 1 \Sigma_{M_*}$–$\Sigma_{\rm SR}$ Law

Figure 20 reinterprets Figure 7's top and middle right panels using dust-uncorrected EW(Hα+[N II]) as an sSFR proxy (left) and physical—not r_e-normalized—radii (right). These yield very similar trends to those discussed in text and preserve the systems' rank ordering. The exception is CSF's EW profile, where, compared to SED-derived sSFR(r), INNER levels are elevated and larger r values depressed relative to SSF's. The former effect is largely, if not entirely, due to CSF's AGN activity (Figures 2 and 6), and higher-resolution IFU spectroscopy will reveal if the latter is due to increased extinction toward its H II regions or a real suppression of sSFR beyond the factor of $\sim$3 inferred from the full SED.

Finally, Figure 21 plots the full sample's 12 resolved $\Sigma_{\rm SFR}$ and Σ_{M_*} values, a stellar mass reinterpretation of the Schmidt–Kennicutt law (Schmidt 1959; Kennicutt 1998). The left panel shows lognormal inferences, with delayed exponentials at right. While these techniques yield quite different best-fit relations (Equations (4) and (5) below), both are nevertheless similar to previous $z = 0$ IFU-/resolved SED-based estimates: Cano-Díaz et al. (2016) found a slope and dispersion of 0.68 ± 0.04 and 0.23 dex, respectively, corresponding to our delayed exponential results, while Abdurro'uf & Akiyama (2017) found 0.33 and 0.7, respectively, closer to (though with larger scatter than) our lognormal results, highlighting the dependence of such scaling relations on SFH choice.

Using lognormal SFHs, we find

$$\log\left[\frac{\Sigma_{\rm SFR}}{M_\odot\ {\rm yr}^{-1}\,{\rm kpc}^{-2}}\right] = -(0.94 \pm 0.02) + (0.2 \pm 0.1)\log\left[\frac{\Sigma_{M_*}}{10^{8.75}\,M_\odot\ {\rm kpc}^{-2}}\right], \quad (4)$$

with intrinsic scatter $\sigma_{\rm int} = 0.33$ dex.

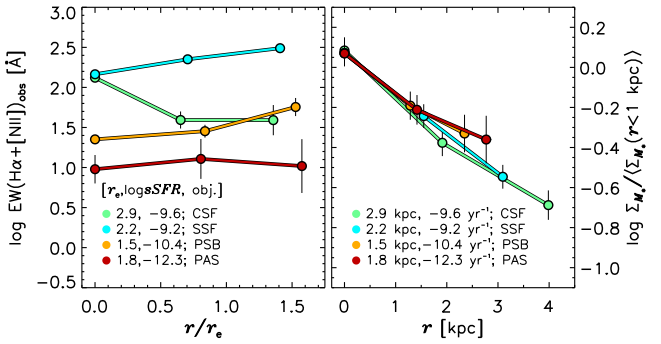

Figure 20. Reinterpretations of Figure 7. Left: dust-uncorrected EW(Hα+[N II]) yields similar trends to SED-fit sSFRs. CSF is an exception: AGN activity elevates the INNER inference (Figures 2 and 6), while those at larger r are $\sim$10$\times$ depressed relative to SSF. The IFU data will reveal if this is due to increased extinction toward CSF's H II regions or a real suppression of sSFR beyond the factor of $\sim$3 inferred from the full SED. Right: inner kpc-normalized Σ_{M_*} profiles vs. physical radii (as opposed to r/r_e), highlighting the sample galaxies' sizes. Trends are the same as in the main-text figure, with the larger star-forming systems having steeper mass profiles than the passive ones, perhaps suggesting that the latter already have some dry merging (Section 4.2; e.g., Newman et al. 2012).

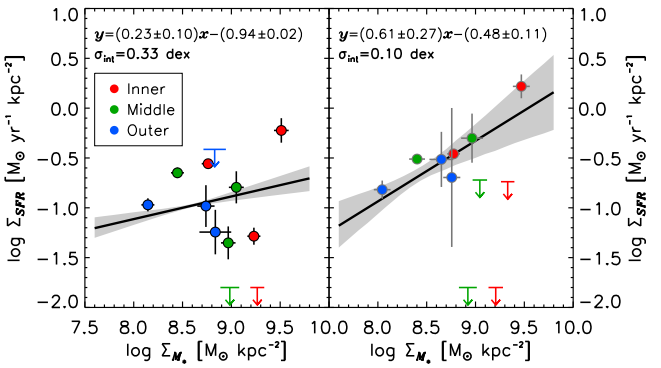

Figure 21. Resolved SFR vs. M_* surface densities (analogous to Schmidt 1959; Kennicutt 1998) assuming lognormal (left) and delayed exponential SFHs (right). Both have $x \equiv \log \Sigma_{M_*} - 8.75$, with linear best fits performed only to detections by bootstrapping and varying points by their x and y error bars. While quite different from each other, both inferences are similar to $z = 0$ IFU/resolved SED estimates over a similar mass (but not Σ_{M_*}) range: Cano-Díaz et al. (2016) found a slope/dispersion of 0.68 ± 0.04 and 0.23 dex, respectively, corresponding to our delayed exponential results; Abdurro'uf & Akiyama (2017) found 0.33 and 0.7, respectively, closer to our lognormal results. This highlights the dependence of scaling relations on SFH choice.

Using delayed exponentials yields

$$\log\left[\frac{\Sigma_{\rm SFR}}{M_\odot\ {\rm yr}^{-1}\,{\rm kpc}^{-2}}\right] = -(0.48 \pm 0.11) + (0.6 \pm 0.3)\log\left[\frac{\Sigma_{M_*}}{10^{8.75}\,M_\odot\ {\rm kpc}^{-2}}\right], \quad (5)$$

with intrinsic scatter $\sigma_{\rm int} = 0.10$ dex.

ORCID iDs

L. E. Abramson https://orcid.org/0000-0002-8860-1032
A. B. Newman https://orcid.org/0000-0001-7769-8660
T. Treu https://orcid.org/0000-0002-8460-0390
T. Morishita https://orcid.org/0000-0002-8512-1404
X. Wang https://orcid.org/0000-0002-9373-3865
A. Hoag https://orcid.org/0000-0001-8989-2567
K. B. Schmidt https://orcid.org/0000-0002-3418-7251
C. A. Mason https://orcid.org/0000-0002-3407-1785
M. Bradač https://orcid.org/0000-0001-5984-0395
G. B. Brammer https://orcid.org/0000-0003-2680-005X
A. Dressler https://orcid.org/0000-0002-6317-0037
B. M. Poggianti https://orcid.org/0000-0001-8751-8360
M. Trenti https://orcid.org/0000-0001-9391-305X
B. Vulcani https://orcid.org/0000-0003-0980-1499

References

Abdurro'uf, & Akiyama, M. 2017, MNRAS, 469, 2806
Abramson, L. E., Gladders, M. D., Dressler, A., et al. 2015, ApJL, 801, L12
Abramson, L. E., Gladders, M. D., Dressler, A., et al. 2016, ApJ, 832, 7
Abramson, L. E., Kelson, D. D., Dressler, A., et al. 2014, ApJL, 785, L36
Abramson, L. E., & Morishita, T. 2018, ApJ, 858, 40
Aird, J., Coil, A. L., Moustakas, J., et al. 2012, ApJ, 746, 90
Allen, J. T., Croom, S. M., Konstantopoulos, I. S., et al. 2015, MNRAS, 446, 1567
Barro, G., Faber, S. M., Koo, D. C., et al. 2017a, ApJ, 840, 47
Barro, G., Faber, S. M., Pérez-González, P. G., et al. 2013, ApJ, 765, 104
Barro, G., Kriek, M., Pérez-González, P. G., et al. 2017b, ApJ, 840, 47
Bell, E. F., van der Wel, A., Papovich, C., et al. 2012, ApJ, 753, 167
Belli, S., Newman, A. B., & Ellis, R. S. 2017, ApJ, 834, 18
Benson, A. J. 2012, NewA, 17, 175
Bertin, E., & Arnouts, S. 1996, A&AS, 117, 393
Bezanson, R., van Dokkum, P. G., Tal, T., et al. 2009, ApJ, 697, 1290
Blanc, G. A., Heiderman, A., Gebhardt, K., Evans, N. J., II, & Adams, J. 2009, ApJ, 704, 842
Brammer, G. B., van Dokkum, P. G., & Coppi, P. 2008, ApJ, 686, 1503
Brammer, G. B., van Dokkum, P. G., Franx, M., et al. 2012, ApJS, 200, 13
Bruzual, G., & Charlot, S. 2003, MNRAS, 344, 1000
Bundy, K., Bershady, M. A., Law, D. R., et al. 2015, ApJ, 798, 7
Calvi, R., Poggianti, B. M., & Vulcani, B. 2011, MNRAS, 416, 727
Calzetti, D., Armus, L., Bohlin, R. C., et al. 2000, ApJ, 533, 682
Caminha, G. B., Grillo, C., Rosati, P., et al. 2017, A&A, 600, A90
Cano-Díaz, M., Sánchez, S. F., Zibetti, S., et al. 2016, ApJL, 821, L26
Cappellari, M., Emsellem, E., Krajnović, D., et al. 2011, MNRAS, 413, 813
Castellano, M., Amorín, R., Merlin, E., et al. 2016, A&A, 590, A31
Ciesla, L., Elbaz, D., & Fensch, J. 2017, A&A, 608, A41
Couch, W. J., & Sharples, R. M. 1987, MNRAS, 229, 423
Croton, D. J., Springel, V., White, S. D. M., et al. 2006, MNRAS, 365, 11
Davé, R., Oppenheimer, B. D., & Finlator, K. 2011, MNRAS, 415, 11
Diemer, B., Sparre, M., Abramson, L. E., & Torrey, P. 2017, ApJ, 839, 26
Domínguez Sánchez, H., Pérez-González, P. G., Esquej, P., et al. 2016, MNRAS, 457, 3743
Dressler, A. 1980, ApJ, 236, 351
Dressler, A., & Abramson, L. 2015, in IAU Symp. 311, Galaxy Masses as Constraints of Formation Models, ed. M. Cappellari & S. Courteau (Cambridge: Cambridge Univ. Press), 140
Dressler, A., & Gunn, J. E. 1983, ApJ, 270, 7
Dressler, A., Kelson, D. D., Abramson, L. E., et al. 2016, ApJ, 833, 251
Dressler, A., Kelson, D. D., & Abramson, L. E. 2018, arXiv:1805.04110
Dressler, A., Oemler, A., Jr., Poggianti, B. M., et al. 2004, ApJ, 617, 867
Dutton, A. A., Conroy, C., van den Bosch, F. C., Prada, F., & More, S. 2010, MNRAS, 407, 2
Eggen, O. J., Lynden-Bell, D., & Sandage, A. R. 1962, ApJ, 136, 748
Fagioli, M., Carollo, C. M., Renzini, A., et al. 2016, ApJ, 831, 173
Feroz, F., & Hobson, M. P. 2008, MNRAS, 384, 449
Förster Schreiber, N. M., Genzel, R., Bouché, N., et al. 2009, ApJ, 706, 1364
Fritz, J., Poggianti, B. M., Bettoni, D., et al. 2007, A&A, 470, 137
Fritz, J., Poggianti, B. M., Cava, A., et al. 2014, A&A, 566, A32
Gadotti, D. A. 2009, MNRAS, 393, 1531
Gallagher, J. S., III, Hunter, D. A., & Tutukov, A. V. 1984, ApJ, 284, 544
Gallazzi, A., Bell, E. F., Zibetti, S., Brinchmann, J., & Kelson, D. D. 2014, ApJ, 788, 72
Gallazzi, A., Charlot, S., Brinchmann, J., White, S. D. M., & Tremonti, C. A. 2005, MNRAS, 362, 41
Garrison-Kimmel, S., Hopkins, P. F., Wetzel, A., et al. 2017, arXiv:1712.03966
Genel, S., Nelson, D., Pillepich, A., et al. 2018, MNRAS, 474, 3976
Gladders, M. D., Oemler, A., Dressler, A., et al. 2013, ApJ, 770, 64
Goddard, D., Thomas, D., Maraston, C., et al. 2017, MNRAS, 466, 4731
Grillo, C., Suyu, S. H., Rosati, P., et al. 2015, ApJ, 800, 38

Grogin, N. A., Kocevski, D. D., Faber, S. M., et al. 2011, ApJS, 197, 35
Guglielmo, V., Poggianti, B. M., Moretti, A., et al. 2015, MNRAS, 450, 2749
Harrison, C. M. 2014, in IAU Symp. 304, Multiwavelength AGN Surveys and Studies, ed. A. M. Mickaelian & D. B. Sanders (Cambridge: Cambridge Univ. Press), 284
Hoag, A., Huang, K.-H., Treu, T., et al. 2016, ApJ, 831, 182
Hopkins, P. F., Kereš, D., Oñorbe, J., et al. 2014, MNRAS, 445, 581
Horne, K. 1986, PASP, 98, 609
Illingworth, G., Magee, D., Bouwens, R., et al. 2016, arXiv:1606.00841
Iyer, K., & Gawiser, E. 2017, ApJ, 838, 127
Jauzac, M., Clément, B., Limousin, M., et al. 2014, MNRAS, 443, 1549
Johnson, T. L., Rigby, J. R., Sharon, K., et al. 2017a, ApJL, 843, L21
Johnson, T. L., Sharon, K., Bayliss, M. B., et al. 2014, ApJ, 797, 48
Johnson, T. L., Sharon, K., Gladders, M. D., et al. 2017b, ApJ, 843, 78
Jones, T., Wang, X., Schmidt, K. B., et al. 2015, AJ, 149, 107
Juneau, S., Bournaud, F., Charlot, S., et al. 2014, ApJ, 788, 88
Kauffmann, G., Heckman, T. M., White, S. D. M., et al. 2003, MNRAS, 341, 33
Kawamata, R., Oguri, M., Ishigaki, M., Shimasaku, K., & Ouchi, M. 2016, ApJ, 819, 114
Kelson, D. D. 2014, arXiv:1406.5191
Kelson, D. D., Benson, A. J., & Abramson, L. E. 2016, arXiv:1610.06566
Kelson, D. D., Illingworth, G. D., Franx, M., & van Dokkum, P. G. 2001, ApJL, 552, L17
Kelson, D. D., Illingworth, G. D., Franx, M., & van Dokkum, P. G. 2006, ApJ, 653, 159
Kelson, D. D., Williams, R. J., Dressler, A., et al. 2014, ApJ, 783, 110
Kennicutt, R. C., Jr. 1998, ApJ, 498, 541
Kepner, J. V. 1999, ApJ, 520, 59
Kriek, M., Shapley, A. E., Reddy, N. A., et al. 2015, ApJS, 218, 15
Kriek, M., van der Wel, A., van Dokkum, P. G., Franx, M., & Illingworth, G. D. 2008, ApJ, 682, 896
Lang, P., Wuyts, S., Somerville, R. S., et al. 2014, ApJ, 788, 11
Larson, R. B., Tinsley, B. M., & Caldwell, C. N. 1980, ApJ, 237, 692
Lee, S.-K., Ferguson, H. C., Somerville, R. S., Wiklind, T., & Giavalisco, M. 2010, ApJ, 725, 1644
Lee-Brown, D. B., Rudnick, G. H., Momcheva, I. G., et al. 2017, ApJ, 844, 43
Lilly, S. J., & Carollo, C. M. 2016, ApJ, 833, 1
Lotz, J. M., Koekemoer, A., Coe, D., et al. 2017, ApJ, 837, 97
Ma, C.-P., Greene, J. E., McConnell, N., et al. 2014, ApJ, 795, 158
Madau, P., & Dickinson, M. 2014, ARA&A, 52, 415
Magdis, G. E., Bureau, M., Stott, J. P., et al. 2016, MNRAS, 456, 4533
Markwardt, C. B. 2009, in ASP Conf. Ser. 411, Astronomical Data Analysis Software and Systems XVIII, ed. D. A. Bohlender, D. Durand, & P. Dowler (San Francisco, CA: ASP), 251
Mason, C. A., Treu, T., Fontana, A., et al. 2017, ApJ, 838, 14
McAlpine, S., Helly, J. C., Schaller, M., et al. 2016, A&C, 15, 72
McDermid, R. M., Alatalo, K., Blitz, L., et al. 2015, MNRAS, 448, 3484
Momcheva, I. G., Brammer, G. B., van Dokkum, P. G., et al. 2016, ApJS, 225, 27
Morishita, T., Abramson, L. E., Treu, T., et al. 2017, ApJ, 835, 254
Morishita, T., & Ichikawa, T. 2016, ApJ, 816, 87
Morishita, T., Ichikawa, T., Noguchi, M., et al. 2015, ApJ, 805, 34
Muñoz, J. A., & Peeples, M. S. 2015, MNRAS, 448, 1430
Nelson, E. J., van Dokkum, P. G., Förster Schreiber, N. M., et al. 2016a, ApJ, 828, 27
Nelson, E. J., van Dokkum, P. G., Momcheva, I. G., et al. 2016b, ApJL, 817, L9
Newman, A. B., Belli, S., & Ellis, R. S. 2015, ApJL, 813, L7
Newman, A. B., Ellis, R. S., Andreon, S., et al. 2014, ApJ, 788, 51
Newman, A. B., Ellis, R. S., Bundy, K., & Treu, T. 2012, ApJ, 746, 162
Nipoti, C., Treu, T., Leauthaud, A., et al. 2012, MNRAS, 422, 1714
Noeske, K. G., Weiner, B. J., Faber, S. M., et al. 2007, ApJL, 660, L43
Oemler, A., Jr., Abramson, L. E., Gladders, M. D., et al. 2017, ApJ, 844, 45
Oemler, A., Jr., Dressler, A., Gladders, M. G., et al. 2013a, ApJ, 770, 63
Oemler, A., Jr., Dressler, A., Gladders, M. G., et al. 2013b, ApJ, 770, 61
Oguri, M., Takada, M., Okabe, N., & Smith, G. P. 2010, MNRAS, 405, 2215
Pacifici, C., Kassin, S. A., Weiner, B., Charlot, S., & Gardner, J. P. 2013, ApJL, 762, L15
Pacifici, C., Kassin, S. A., Weiner, B. J., et al. 2016, ApJ, 832, 79
Peng, C. Y., Ho, L. C., Impey, C. D., & Rix, H.-W. 2002, AJ, 124, 266
Peng, Y., Maiolino, R., & Cochrane, R. 2015, Natur, 521, 192
Peng, Y.-j., Lilly, S. J., Kovač, K., et al. 2010, ApJ, 721, 193
Poggianti, B. M., Calvi, R., Bindoni, D., et al. 2013, ApJ, 762, 77
Poggianti, B. M., Moretti, A., Gullieuszik, M., et al. 2017, ApJ, 844, 48
Poggianti, B. M., Smail, I., Dressler, A., et al. 1999, ApJ, 518, 576
Postman, M., Coe, D., Benítez, N., et al. 2012, ApJS, 199, 25
Richard, J., Jauzac, M., Limousin, M., et al. 2014, MNRAS, 444, 268
Rigby, J. R., Johnson, T. L., Sharon, K., et al. 2017, ApJ, 843, 79
Salim, S., Rich, R. M., Charlot, S., et al. 2007, ApJS, 173, 267
Salpeter, E. E. 1955, ApJ, 121, 161
Sánchez, S. F., Kennicutt, R. C., Gil de Paz, A., et al. 2012, A&A, 538, A8
Sanders, R. L., Shapley, A. E., Zhang, K., & Yan, R. 2017, arXiv:1708.04625
Schlafly, E. F., & Finkbeiner, D. P. 2011, ApJ, 737, 103
Schmidt, K. B., Treu, T., Brammer, G. B., et al. 2014, ApJL, 782, L36
Schmidt, M. 1959, ApJ, 129, 243
Schreiber, C., Elbaz, D., Pannella, M., et al. 2016, A&A, 589, A35
Shapley, A. E., Reddy, N. A., Kriek, M., et al. 2015, ApJ, 801, 88
Silk, J., & Norman, C. 1981, ApJ, 247, 59
Speagle, J. S., Steinhardt, C. L., Capak, P. L., & Silverman, J. D. 2014, ApJS, 214, 15
Spitler, L. R., Labbé, I., Glazebrook, K., et al. 2012, ApJL, 748, L21
Steidel, C. C., Rudie, G. C., Strom, A. L., et al. 2014, ApJ, 795, 165
Tacchella, S., Carollo, C. M., Renzini, A., et al. 2015, Sci, 348, 314
Tacchella, S., Dekel, A., Carollo, C. M., et al. 2016a, MNRAS, 458, 242
Tacchella, S., Dekel, A., Carollo, C. M., et al. 2016b, MNRAS, 457, 2790
Thomas, D., Maraston, C., Bender, R., & Mendes de Oliveira, C. 2005, ApJ, 621, 673
Tinsley, B. M. 1968, ApJ, 151, 547
Toft, S., Zabl, J., Richard, J., et al. 2017, Natur, 546, 510
Trager, S. C., Faber, S. M., Worthey, G., & González, J. J. 2000, AJ, 120, 165
Trager, S. C., Worthey, G., Faber, S. M., Burstein, D., & Gonzalez, J. J. 1998, ApJS, 116, 1
Treu, T., Ellis, R. S., Liao, T. X., et al. 2005, ApJ, 633, 174
Treu, T., Schmidt, K. B., Brammer, G. B., et al. 2015, ApJ, 812, 114
van de Sande, J., Kriek, M., Franx, M., et al. 2013, ApJ, 771, 85
van der Wel, A., Franx, M., van Dokkum, P. G., et al. 2014, ApJ, 788, 28
van der Wel, A., Noeske, K., Bezanson, R., et al. 2016, ApJS, 223, 29
van Dokkum, P. G., Leja, J., Nelson, E. J., et al. 2013, ApJL, 771, L35
van Dokkum, P. G., Nelson, E. J., Franx, M., et al. 2015, ApJ, 813, 23
Vogelsberger, M., Genel, S., Springel, V., et al. 2014, MNRAS, 444, 1518
Voit, G. M., Bryan, G. L., O'Shea, B. W., & Donahue, M. 2015, ApJL, 808, L30
Vulcani, B., Poggianti, B. M., Fritz, J., et al. 2015a, ApJ, 798, 52
Vulcani, B., Treu, T., Nipoti, C., et al. 2017, ApJ, 837, 126
Vulcani, B., Treu, T., Schmidt, K. B., et al. 2015b, ApJ, 814, 161
Vulcani, B., Treu, T., Schmidt, K. B., et al. 2016, ApJ, 833, 178
Wang, X., Hoag, A., Huang, K.-H., et al. 2015, ApJ, 811, 29
Wang, X., Jones, T. A., Treu, T., et al. 2017, ApJ, 837, 89
Weisz, D. R., Dolphin, A. E., Skillman, E. D., et al. 2014, ApJ, 789, 148
Whitaker, K. E., Franx, M., Leja, J., et al. 2014, ApJ, 795, 104
Whitaker, K. E., van Dokkum, P. G., Brammer, G., et al. 2013, ApJL, 770, L39
Whitaker, K. E., van Dokkum, P. G., Brammer, G., & Franx, M. 2012, ApJL, 754, L29
Williams, R. J., Quadri, R. F., Franx, M., van Dokkum, P., & Labbé, I. 2009, ApJ, 691, 1879
Worthey, G., Faber, S. M., & Gonzalez, J. J. 1992, ApJ, 398, 69
Wuyts, E., Rigby, J. R., Gladders, M. D., et al. 2012a, ApJ, 745, 86
Wuyts, E., Rigby, J. R., Gladders, M. D., & Sharon, K. 2014, ApJ, 781, 61
Wuyts, E., Rigby, J. R., Sharon, K., & Gladders, M. D. 2012b, ApJ, 755, 73
York, D. G., Adelman, J., Anderson, J. E., Jr., et al. 2000, AJ, 120, 1579
Zitrin, A., Broadhurst, T., Umetsu, K., et al. 2009, MNRAS, 396, 1985
Zitrin, A., Meneghetti, M., Umetsu, K., et al. 2013, ApJL, 762, L30
Zolotov, A., Dekel, A., Mandelker, N., et al. 2015, MNRAS, 450, 2327